



# Temporal Characteristics of P-Band Tomographic Radar Backscatter of a Boreal Forest

Albert R. Monteith , *Member, IEEE*, and Lars M. H. Ulander , *Fellow, IEEE*

**Abstract**—Temporal variations in synthetic aperture radar (SAR) backscatter over forests are of concern for any SAR mission with the goal of estimating forest parameters from SAR data. In this article, a densely sampled, two-year long time series of P-band (420 to 450 MHz) boreal forest backscatter, acquired by a tower-based radar, is analyzed. The experiment setup provides time series data at multiple polarizations. Tomographic capabilities allow the separation of backscatter at different heights within the forest. Temporal variations of these multipolarized, tomographic radar observations are characterized and quantified. The mechanisms studied are seasonal variations, effects of freezing conditions, diurnal variations, effects of wind, and the effects of rainfall on backscatter. An emphasis is placed on upper-canopy backscatter, which has been shown to be a robust proxy for forest biomass. The canopy backscatter was more stable than ground-level backscatter during nonfrozen conditions, supporting forest parameter retrieval approaches based on tomography or interferometric ground notching. Large backscatter variations during frozen conditions, which may be detected using cross-polarized backscatter observations, can result in large errors in forest parameter estimates. Diurnal backscatter variations observed during hot periods were likely connected to tree water transport and storage mechanisms. Backscatter changes were also observed during strong winds. These variations were small in comparison to the variations due to freeze-thaw and soil moisture changes and should not result in significant forest parameter estimation errors. The presented results are useful for designing physically based and semiempirical scattering models that account for temporal changes in scattering characteristics.

**Index Terms**—Backscatter, boreal forest, p-band, time series.

## I. INTRODUCTION

**F**OREST backscatter measured using imaging radars varies with time due to changes in weather conditions, particularly pronounced at higher latitudes due to strong seasonal effects [1]–[4]. If such variations are not accounted for, they may affect the accuracy of forest parameter estimates such as forest height and biomass, as estimated from synthetic aperture radar (SAR) data.

Manuscript received April 3, 2020; revised June 7, 2020, July 22, 2020, September 16, 2020, and November 10, 2020; accepted December 27, 2020. Date of publication January 11, 2021; date of current version January 29, 2021. This work was supported in part by the Hildur and Sven Wingquist Foundation for Forest Research, in part by the European Space Agency (ESA), and in part by the Swedish National Space Agency. (*Corresponding author: Albert R. Monteith.*)

Albert R. Monteith is with the Department of Space, Earth, and Environment, Chalmers University of Technology, SE-412 96 Gothenburg, Sweden (e-mail: albert.monteith@chalmers.se).

Lars M. H. Ulander is with the Department of Space, Earth, and Environment, Chalmers University of Technology, SE-412 96 Gothenburg, Sweden, and also with the Radar Systems Unit, Swedish Defence Research Agency (FOI), SE-581 11 Linköping, Sweden (e-mail: lars.ulander@chalmers.se).

Digital Object Identifier 10.1109/JSTARS.2021.3050611

The European Space Agency’s BIOMASS SAR satellite is scheduled for launch in 2023. The main scientific objective of the mission is to quantify forest carbon stocks and fluxes through the mapping of above-ground biomass from SAR observations [5], [6]. The BIOMASS SAR instrument will be the first ever spaceborne SAR operating at P-band (centered at 435 MHz). This relatively low frequency, compared to existing spaceborne SARs, allows the emitted electromagnetic waves to penetrate the canopy and reflect off larger structures such as branches and tree stems, where the majority of a tree’s biomass is located. This makes P-band especially sensitive to above-ground forest biomass [7]–[9]. A consequence of the increased canopy penetration is that the ground contributes significantly to the total backscattered field, either through direct rough surface scattering or double-bounce scattering by the ground and tree trunks [10]. Variations in ground roughness, slope and soil moisture can thus introduce a significant bias in the estimated biomass [11]. The BIOMASS mission is designed for fully polarimetric, interferometric, and tomographic imaging. Due to P-band transmission regulations over Europe and North America, all of the world’s forests will not be covered by BIOMASS. The loss in terms of the global forest above-ground biomass carbon stock is estimated to be 18.2%, whereas the corresponding value for boreal forests is 36.7% [12]. In boreal forests, the combination of polarimetric channels in SAR observations have been shown to reduce the influence of the ground [13]. In tropical forests, tomographic intensity near 30-m above the ground was shown to be less impacted by terrain topography and closely correlated with forest biomass [14]. Tomographic ground separation has also been achieved in boreal forests [15]. More recently, a ground-cancelling technique was developed whereby the ground contribution is suppressed by coherently combining interferometric image pairs, isolating the above-ground canopy contribution [16], [17]. Central to all these biomass estimation approaches is the use of the measured backscatter, especially that of the above-ground canopy, to estimate biomass. Even with the ground component removed, the canopy backscatter does not uniquely depend on biomass. Changes in canopy backscatter due to weather and seasonal changes will affect the estimated biomass. Very little is known about the characteristics of such temporal variations, especially in boreal forests, making it difficult to design biomass estimation algorithms that are robust to temporal variations. The lack of a quantitative understanding of environmentally induced backscatter variations is also the main issue in developing algorithms for forest degradation detection [11].

Forest backscatter observed by a SAR is governed by the geometry of forest structures (ground, stems, branches, and leaves/needles) and the relative permittivities of these structures [18]. The geometry and permittivity determine the angular distribution and strength of these reflections as well as the absorption of electromagnetic energy in forest structures. Backscatter variations occur due to changes in either the geometry or permittivity of forest structures.

Apart from tree growth, geometric changes occur mainly due to wind-induced tree swaying. The resulting displacement of scatterers can be close to, or larger than, the wavelength, and thus will affect the scattered field measured by a radar. To a lesser extent, terrestrial lidar observations have shown that geometric changes occur due to diurnal drooping and rising of branches [19]. Geometric changes therefore occur at timescales of seconds (wind) to years (tree growth).

For most cases, an increase in the permittivity of the soil or vegetation increases the forest backscatter [20]. Changes in the permittivity of forest structures have been observed to be caused by a variety of mechanisms that affect the water content and chemical composition of forest materials [21]. A higher soil water content increases the permittivity of the soil and results in a stronger ground reflection [22]–[24]. Mechanisms driving water content variations in trees are significantly more complex. The most widely accepted theory of water transport in trees is the cohesion-tension theory [25]. According to the cohesion-tension theory, water moves from the roots to the stomata (pores in leaves/needles for gas exchange with the atmosphere) as continuous columns of water, as water is drawn out of stomata during transpiration. The flow of water from roots to stomata can be characterized by resistances, limiting the rate of upward flow, and capacitances, representing water storages in the xylem (sapwood) and phloem (bark) [26], [27]. These water reserves are depleted in hot and dry conditions when the rate of transpiration exceeds the rate of soil water uptake, resulting in a change of permittivity of tree structures. The rate of transpiration is controlled by a complicated interaction between solar radiation, air temperature, relative humidity, air pressure, wind speed, CO<sub>2</sub> concentration, soil water availability, and by the trees themselves through stomatal conductance [28], [29]. In freezing conditions, water within the trees freezes, resulting in a significant drop in permittivity. Reversible freezing occurs at different times, temperatures, and rates in the various forest structures [30].

The mechanisms by which the permittivity of forest structures vary with time are complex and are currently not fully understood. Our lack of knowledge of how trees respond to their environment can be attributed to the laborious, indirect, invasive, and even destructive nature of measurement techniques for quantifying spatio-temporal tree water content and chemical concentrations. The effects of changing weather and seasonal conditions on forest backscatter can currently only be revealed by empirical studies. Existing P-band observation data of boreal forests are limited to that of a few airborne campaigns [31]–[35]. These observations lack the temporal diversity necessary for investigating the temporal characteristics of P-band backscatter.

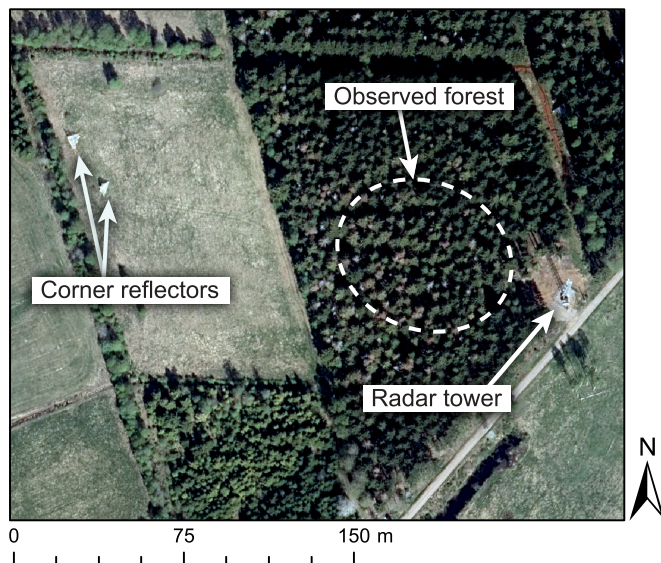


Fig. 1. RGB aerial photo of the experiment site acquired on 10 May 2018 by the Swedish National Land Survey (Lantmäteriet). The bottom corner reflector was used for calibrating the tower radar and the top corner reflector was temporarily installed for airborne SAR observations.

In this study, a boreal forest stand was observed using a tower-based multipolarimetric, tomographic P-band radar. The aims of the study were to:

- 1) collect densely sampled time series of backscatter from different height intervals within the forest canopy;
- 2) identify the most significant temporal features in the dataset; and
- 3) gain insight into the relationship between backscatter, meteorological variables, and ecophysiological mechanisms.

The goal of the experiment is to gain a better understanding of the electromagnetic scattering mechanisms taking place during SAR observations and how SAR observations are affected by changing weather and seasonal conditions.

The rest of this article is organized as following. The experiment is described in Section II and data analysis methods are detailed in Section III. Section IV contains the first result analysis of the dataset, then a discussion of the results and their implications on forest parameter retrieval is given in Section V.

## II. EXPERIMENT DESCRIPTION

### A. Experiment Site

The observed forest is a homogeneous, mature stand of Norway spruce [*Picea abies* (L.) Karst]. The forest stand is located in the Remningstorp experimental forest in southern Sweden and had an above-ground biomass density of 250 tons/ha in the fall of 2014 [4]. The terrain is flat, is covered in moss, and has little understory. The canopy height varies from 25 to 27 m. The 50-m high radar tower is located at the edge of the forest stand (58° 27' 5" N, 13° 37' 35" E) as shown in Fig. 1. Several trihedral corner reflectors are placed around the site for calibration purposes.

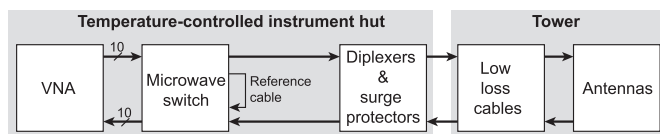


Fig. 2. Block diagram of the radar instrument.

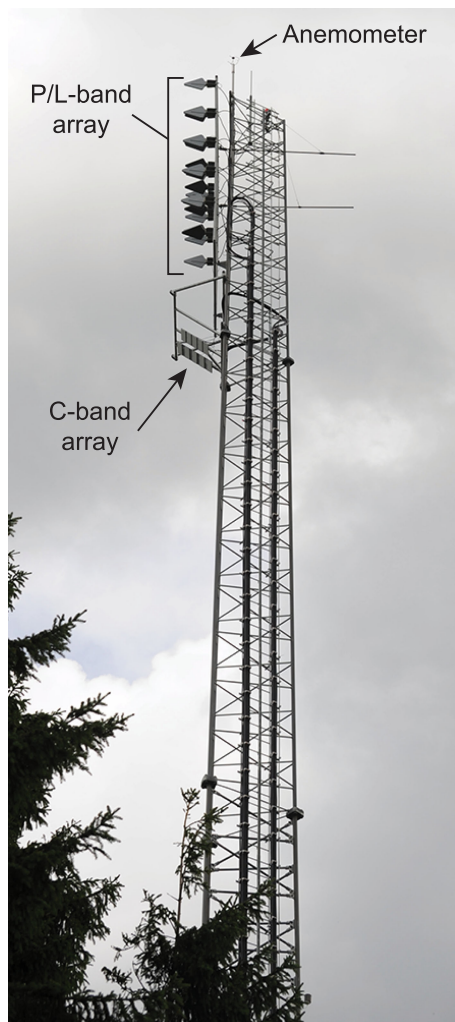


Fig. 3. Photo of the top section of the radar tower. The two antenna arrays were connected to the VNA on the ground via coaxial cables.

### B. Radar Instrument

The radar instrument consists of a vector network analyzer (VNA) connected to an antenna array (see Fig. 2). The VNA has 20 ports, each of which is connected to one of the 20 antennas (10 transmit and 10 receive) in the array at the top of the tower (see Fig. 3). The VNA operates by transmitting, from a single VNA port, monochromatic pulses over a range of frequencies in discrete frequency steps. The stepped-frequency sweep covers a bandwidth of 30 MHz centered at 435 MHz. The signal is emitted in frequency steps of 0.5 MHz. These signal parameters result in a range resolution of 5 m and a maximum unambiguous range of 300 m. The signal is emitted as an electromagnetic wave from a single antenna and scatters off the scene producing a scattered

wave. The scattered wave is sampled in space by all 20 antennas in the array simultaneously. This parallel measurement configuration greatly reduces the measurement time compared to systems employing mechanical switching between antennas [36]. The antenna array was designed for tomographic imaging of the forest scene below at P-band to L-band (1270 MHz) for all linear polarization combinations (HH, VV, HV, and VH). A second array is used for C-band (5410 MHz) measurements. Note that the design of the antenna array implies different antenna patterns and phase centers for the different polarization combinations. A specific calibration procedure would be needed to exploit the polarimetric phases and fully polarimetric data. Such nontrivial calibration procedure would require a specific study, so that we prefer to focus here on the intensities derived for the abovementioned combination of polarization states. Details of the array designs are given in [36] and [37]. The close antenna spacing and finite-bandwidth VNA measurements result in mutual antenna coupling, which adds distortion to the received signals. The mutual coupling component of the received signal was suppressed, without affecting the spatial resolution, using a novel procedure described in [38]. The microwave switch in Fig. 2 is a mechanical switch used only for internal calibration purposes using a reference cable.

### C. Temporal Stability of the Radar Instrument

Temporal variations in the total gain of the signal chain must be insignificant compared to variations in the forest backscatter if temporal variations in the forest backscatter are to be studied. To minimize the influence of weather conditions on the system response, all active electronics were housed in a temperature-controlled hut, antennas with weather-resistant radomes were selected and all outdoor connections were sealed with vulcanizing tape. The tower was designed and constructed for a maximum horizontal deflection at the tower top of  $\pm 3$  cm for wind speeds up to 17 m/s. To assess the temporal stability of the VNA's measurement response, each transmitting port was connected to each receiving port via the reference cable (see Fig. 2) at least once every hour. An example of the insertion loss and phase shift measured through the reference cable between two VNA ports is shown in Fig. 4. An insignificant amount of magnitude and phase variation was observed, indicating that the VNA measurement response was stable for the duration of the experiment.

To assess the temporal stability of the low-loss cables and antennas on the tower, the mutual coupling components between antennas and the response from a trihedral corner reflector were analyzed, as was done in [4]. The corner reflector was placed on an open field and in direct line of sight of the radar antennas. Fig. 5 shows the mutual coupling power and forest reflectivity as measured from an HH-polarized range profile. The mutual coupling power shows significantly less temporal variation compared to the forest reflectivity, indicating that the system's gain response is stable enough for studying forest backscatter variations. The magnitude response from the trihedral corner reflector showed more variation than that of the mutual coupling component, appearing to coincide with freezing temperatures. These variations were not observed in the mutual coupling power,

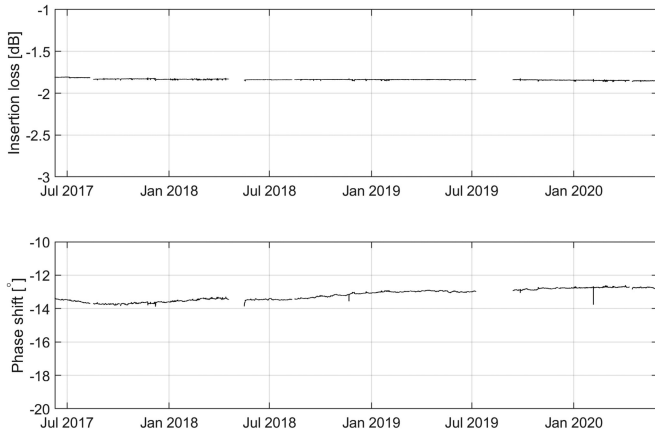


Fig. 4. Example of the insertion loss and phase shift by a reference cable connected between a transmit-receive pair of VNA ports measured at 1-h intervals at 435 MHz. There was very little variation over the duration of the experiment, indicating that there was an insignificant amount of drift in the VNA’s measurement response.

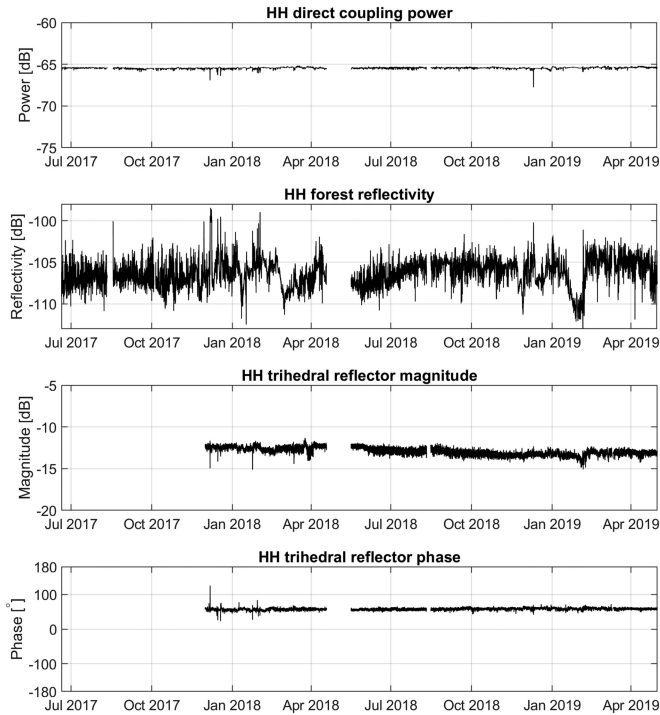


Fig. 5. Examples of the mutual coupling power and forest reflectivity extracted from an HH range profile. The bottom two plots show the corner reflector magnitude and phase for the duration of the experiment. The little variation in the mutual coupling power compared to forest reflectivity variations indicates that there was an insignificant amount of systematic temporal variation in the instrument’s gain. The corner reflector phase was also very stable for the duration of the experiment.

nor in the VV trihedral response, and thus it was concluded that ground-trihedral reflections were the cause of the observed fluctuations in the HH trihedral response. Ground conditions had less of an influence on VV observations because the Brewster effect is significant at the large incidence angle ( $76^\circ$ ) at the corner reflector’s position. The phase of the trihedral corner reflector was stable for the duration of the experiment. These observations

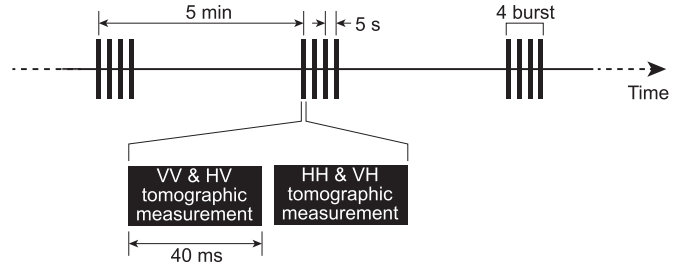


Fig. 6. Timeline of the measurement sequence. Every 5 min, a burst of four tomographic observations were made. Four tomograms for each polarization were thus acquired every 5 min.

indicate that temporal variations in the system response were negligible compared to variations in the forest reflectivity.

#### D. Radar Measurement Sequence

Tomographic image measurements were carried out in bursts of four measurements. The four measurements in a burst were separated by 5 s, and bursts were separated by 5 min (see Fig. 6). Each of the four measurements in a burst covered a tomographic measurement for each polarimetric combination (HH, HV, HH, and VH). VV and HV measurements were done simultaneously. Likewise, HH and VH measurements were done simultaneously. This is possible because the VNA was capable of receiving signals from all 20 antennas in parallel. The measurement time for a single tomographic image was 40 ms, which is short enough for the forest scene to be assumed coherent during a tomographic measurement.

#### E. Meteorological Observations

An on-site weather station measured air temperature, pressure, and relative humidity at heights of 2 and 30-m above ground. The 3-D wind vector was measured by two ultrasonic anemometers installed at the top of the tower (50-m above ground), 20–30 m above the tree tops. Precipitation was measured by a heated rain gauge, which cannot distinguish between rain and snow. Soil temperature and volumetric water content were measured by time-domain reflectometry probes within the upper 30 cm of the soil.

Two surveillance cameras were installed on the tower to observe the state of snow on the canopy and ground. A photo was taken from each camera at 5-min intervals, coinciding with the radar measurements. Snow depth and solar radiation were not measured during this study.

The water vapor pressure deficit (VPD), which is one of the drivers of transpiration, was estimated from the observed air temperature and relative humidity. The saturation pressure of water vapor, which is necessary for estimating the VPD, was estimated using the Goff–Gratch equation [39].

### III. METHOD

#### A. Tomographic Imaging

Tomographic SAR is based on multiple observations of the same scene. Radar observations acquired over a range of azimuth

and elevation angles are coherently combined to construct a 3-D distribution of the backscattered power [40]. This is typically implemented by multiple passes of an airborne or spaceborne radar with different incidence angles. The antenna array in this study has a vertical aperture, providing fine resolution in the ground range-height plane only. Tomographic images were formed in this plane. Azimuth resolution is determined by the antenna gain patterns, resulting in a variable resolution cell size throughout the image plane. This variable resolution cell size introduces a systematic gain which is dependent on the antenna gain patterns, antenna array geometry, and signal parameters. This systematic gain was compensated for by normalizing the backscatter of each pixel by the energy of the image impulse response function for the respective pixel [38].

Tomographic images were constructed from the VNA measurements using a backprojection algorithm [38]. To produce a focused tomographic image, it is necessary that the systematic phase differences between transmit-receive measurements contributing to the backprojection sum are small. Such phase, and also magnitude, imbalances were estimated and compensated for using a trihedral corner reflector as an external reference using a method detailed in [38]. This method is robust to temporal variations in the reflector's reflectivity (e.g., due to time-variant ground-reflector contributions) as long as the system's response is stable, as was concluded in Section II-C.

Examples of tomographic images are shown in Fig. 7. Each image exhibits speckle, which is a result of the coherent addition of scattering contributions from several elements within a resolution cell. Therefore, conclusions about the forest backscatter should not be drawn by directly analyzing the tomograms. The trihedral corner reflector lies on the ground at a ground range of 207 m, where the HH and VV tomograms show bright spots. The HV and VH images are different because different bistatic antenna pairs were used in the measurements. However, the trihedral corner reflector is also slightly visible in the HV image, which indicates that there may be some cross-talk leakage for HV measurements. The reason for this observation is presently unclear, and the HV images were therefore not analyzed in this study. Cross-polarization data are therefore estimated in this study through the VH channel, which would be equal to HV tomographic images for a monostatic radar, assuming target reciprocity. Different antennas were used for HV and VH measurements.

The main forest region of interest (ROI) lies within a ground range of 20 to 70 m of the tower, covering similar incidence angles as space-borne SARs ( $20^\circ$  to  $55^\circ$ ). This region, indicated by the dotted rectangle in Fig. 7, is free from forest edges and corner reflectors. The forest reflectivity distribution for this region peaks at two heights for all polarizations: At the upper canopy (10 to 30-m height) and at the ground level (-10 to 10-m height). Reflections at the upper canopy level are mainly due to volume scattering and apparent reflections at the ground level are mainly due to the sum of direct ground scattering and double-bounce scattering (ground trunk and trunk-ground) [15], [34]. These observations motivate a study of the backscatter mainly within these regions. The forest observed in this experiment is dense,

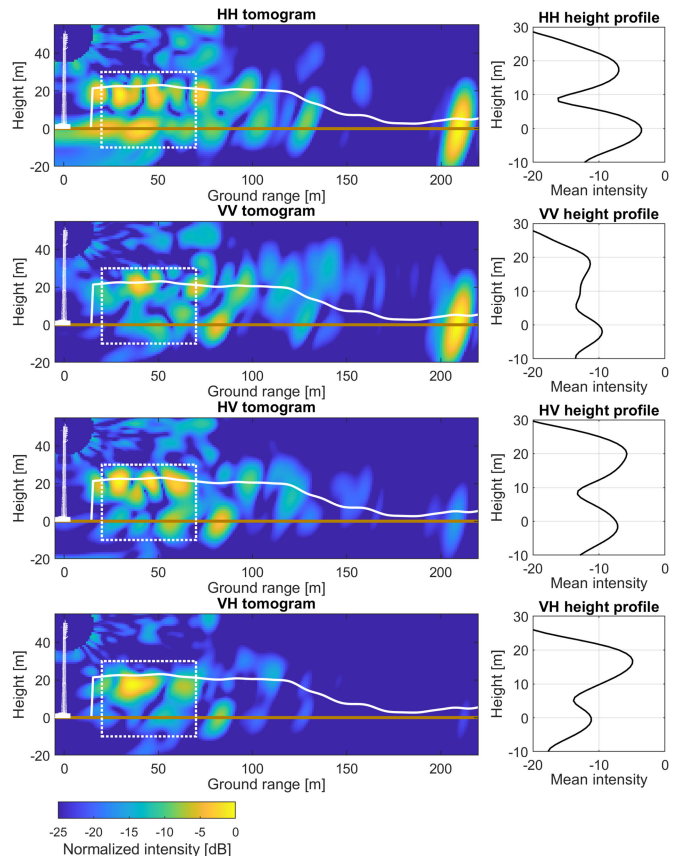


Fig. 7. Tomographic image examples from 06:00 on 1 September 2018. Height profiles of the image backscatter within the regions surrounded by dotted lines are shown on the right of each tomogram. Backscatter peaks at the ground level and upper canopy level. The solid white line shows a lidar-derived canopy height estimate, the brown line shows the ground level and the 50-m high tower is illustrated to scale on the left in each tomogram.

TABLE I  
DEFINITION OF ROIS IN TOMOGRAPHIC IMAGES

ROI	Ground range interval	Height interval	Number of looks
Canopy	20 to 70 m	10 to 30 m	12.8
Ground	20 to 70 m	-10 to 10 m	9.3
Full forest	20 to 70 m	-10 to 30 m	19.7

resulting in a strong canopy contribution and attenuating the ground contribution.

### B. Regions of Interest

Temporal variation of backscatter in the tomographic images was studied using the incoherently integrated pixel intensities in three ROIs as defined in Table I. This was done to simplify the analysis of temporal variations by reducing the dimensionality of the data and, to obtain more accurate estimates of the backscatter. The ROIs are shown in Fig. 8 in the image plane. Estimation accuracy of the image backscatter must be improved by averaging over ROIs because the tomographic images exhibit speckle,

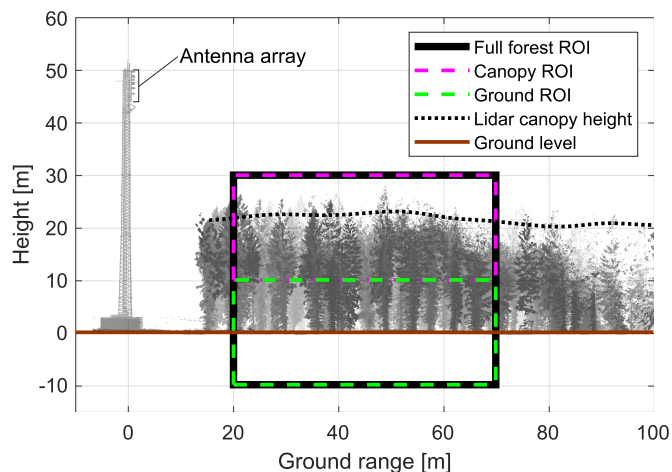


Fig. 8. Diagram (to scale) showing the three ROIs on the image plane in relation to the tower and forest geometry. The tower and forest visualization were produced by a terrestrial lidar scan in 2017 by the Swedish University of Agricultural Sciences (SLU). The canopy height estimate is the 99th percentile from an airborne lidar scan in 2014.

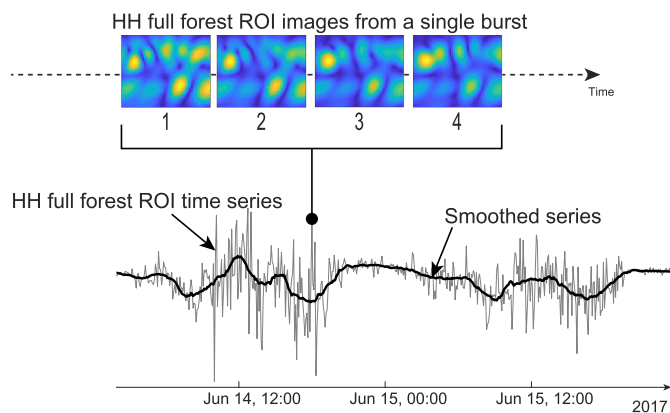


Fig. 9. Illustration of how time series were formed. The backscatter of four tomographic images was incoherently averaged to produce a single sample in a time series. The time series was further smoothed to reveal variations over longer timescales.

whereby a large variance is associated with the backscatter estimate for a single pixel [41]. The backscatter within an ROI was incoherently integrated to yield a lower-variance estimate (higher number of looks) of the mean backscatter within the ROI. To further increase the number of looks, the backscatter estimates from all four consecutive measurements in a burst (Fig. 6) were averaged. Under calm conditions, the four tomographic images are nearly identical, and thus no gain in the number of looks is achieved. In dynamic conditions, such as during wind or rain, these four images will be different due to scattering changes between image acquisitions, and the number of looks will be up to four times the estimates in Table I. The result is a multilooked backscatter time series for each polarization (HH, VV, and VH) in each ROI (full forest, canopy, and ground) with a sampling interval of 5 min. This procedure is illustrated in Fig. 9.

### C. Time Series

Six time series were analyzed: 3 polarizations (HH, VV, and VH) for each of the three ROIs (canopy, ground, and full forest). The time series exhibit variations at timescales of minutes (due to wind-induced movement) to years (due to seasons). The longer the timescale of interest, the more the time series must be temporally smoothed. For example, wind-induced variations obscure diurnal variations, so wind-induced variations must be smoothed to analyze diurnal variations (see Fig. 9). Unless otherwise stated, samples were averaged over 4 h (48 samples). The Savitzky–Golay filter was used to suppress short-term variations while preserving transients [42], which occur due to different mechanisms (e.g., rain and freezing).

All times in this article are local solar times (UTC+54.5 min for the site's longitude). In local solar times, the sun is highest in the sky at 12:00 every day. This is helpful when analyzing biological responses to diurnal variations in solar radiation.

The backscatter time series were not calibrated in an absolute manner using the trihedral corner reflector because its response was affected by the conditions of the surrounding soil. Instead, a preliminary radiometric calibration was done using an airborne SAR as a reference [43]. This calibration was only based on HH observations, and thus the absolute backscatter levels of different polarizations were not compared in this study.

### D. Statistical Inference

The observations in this experiment are subjected to a low number of looks. This is a consequence of the permissible transmit bandwidth (30 MHz), the number of antennas in the array (vertical array aperture), and the limited field of view from the tower. As a result, temporal variations in the spatially averaged backscatter due to speckle may be larger than the physical backscatter variations under study. In order to avoid incorrect conclusions, the expected backscatter variations due to speckle must be quantified and their effect in the temporal domain must be understood. A simulation was used to estimate the number of looks, derive confidence intervals, study the effect of speckle in the time domain, and to develop a method for detecting periods under which the observations show true physical variations in backscatter.

Tomographic images of a uniformly distributed cloud of 5000 point scatterers within the full forest ROI were simulated. The simulation took into account the signal properties, antenna gain patterns, antenna array geometry, and image reconstruction method [38]. To estimate the number of looks, 1000 images were simulated, each with a different realization of point scatterers. For each of the 1000 images, the backscatter over the three ROIs defined in Table I was estimated. These backscatter estimates were then used to estimate the equivalent number of looks [44]. Table I lists the estimated number of looks for each ROI. Fully developed speckle was assumed, which is a reasonable assumption for forest canopies and the large azimuth antenna beamwidth [41]. Even though the areas of the canopy and ground ROIs are the same, the estimated number of looks is lower for the ground region. This is because the resolution in elevation

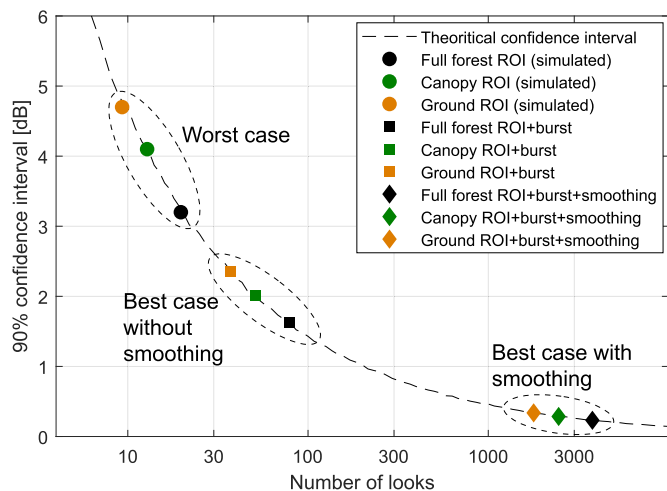


Fig. 10. Theoretical confidence intervals (90%) of backscatter observations due to speckle. Averaging over bursts and smoothing time series over time increases the numbers of looks, making the confidence interval narrower.

is slightly poorer closer to the ground compared to the canopy, which is a result of the antenna array geometry.

The simulation results were also used to estimate 90% confidence intervals for backscatter variations due to speckle. These are plotted in Fig 10. According to the simulation, backscatter variations in the canopy ROI due to speckle lie within a range of approximately 4 dB for 90% of observations. Incoherently averaging over 4 bursts will increase the number of looks by a factor of 4, decreasing the confidence interval to 2 dB. This is assuming windy conditions, under which each burst will provide an independent sample. Smoothing over 4 h will further reduce the confidence interval to below 0.5 dB. These measures appear problematic for observing backscatter variations on the order of 1 dB, such as diurnal cycles [2], unless the conditions are windy and a high number of looks is attained. However, these measures are based on the Rayleigh fading model, which is normally applied to spatial backscatter statistics (e.g., pixels in a SAR image). Extending these statistics to the temporal domain, in which the same forest site is observed over time, is not straightforward because geometric changes depend on environmental conditions. Therefore, the simulation was used to study the statistical characteristics of temporal variations.

The decrease in tree water content during hot days is expected to cause a drop in the canopy backscatter around noon. The radar cross section of each point scatterer in the canopy ROI was modeled as a sinusoid with a peak-to-peak magnitude of 1 dB, reaching a minimum at 12 P.M. A different random component (normally distributed with a standard deviation of 0.2 dB) was added to the sinusoidal component every 5 min to model unequal backscatter variations in the forest. One realization of the radar cross section for a single point scatterer is shown in Fig. 11. The resulting smoothed backscatter time series from 50 different point scatterer position realizations are shown in Fig. 12 (top left). Although there is a large variation when considering multiple realizations of point scatterer positions (e.g., pixels in a

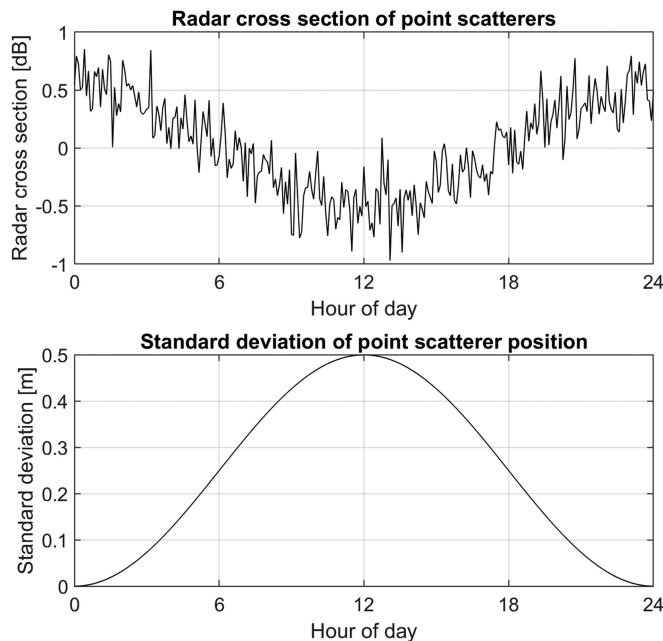


Fig. 11. Example of the radar cross section of a point scatterer (top) and the standard deviation of point scatterer positions (bottom) used as simulation inputs.

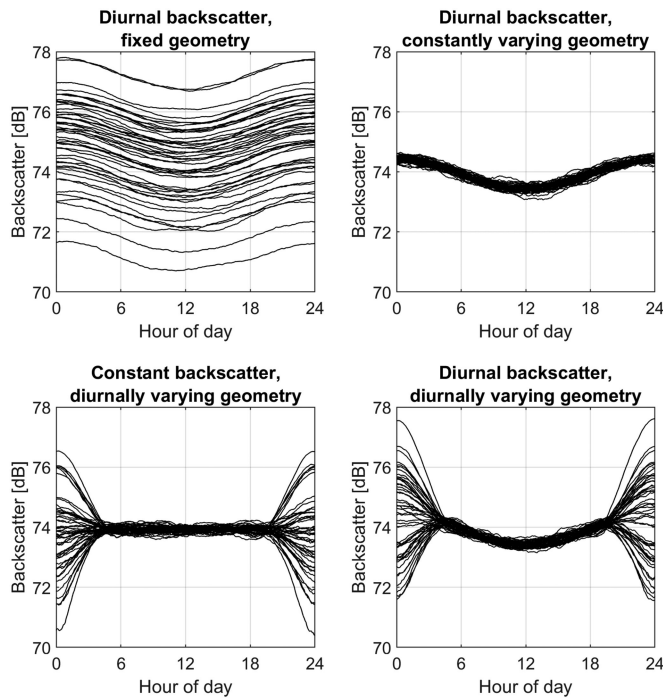


Fig. 12. Simulation results of backscatter time series from 50 different point scatterer scene realizations.

SAR image), the time series for any single geometric realization shows the correct 1 dB backscatter variation.

To investigate the effect of wind on backscatter time series, a random component (normally distributed with a standard deviation of 0.5 m) was added to the point scatterer positions for every tomogram simulated. This resulted in the smoothed time series

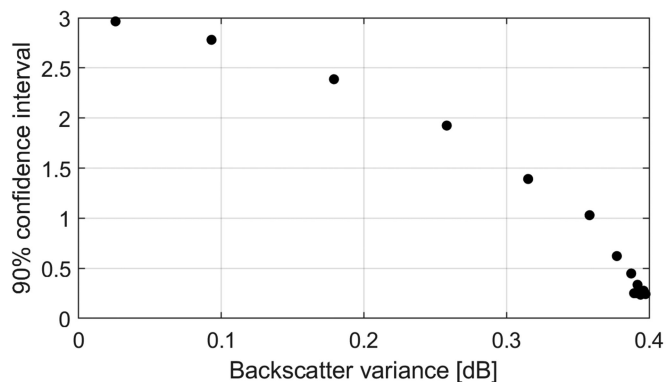


Fig. 13. Simulated relationship between the backscatter variance over a 4-h interval of unsmoothed time series and the 90% confidence interval of speckle variations for the canopy ROI.

shown in Fig. 12 (top right). The decorrelation caused by the fluctuating geometry increases the number of looks, decreasing the variance between the 50 different point scatterer realizations. The time series for any forest realization again shows the correct 1-dB backscatter variation.

Strong winds rarely persist for entire days. During the summer, convective winds are common, in which the wind speed is high during the day and low during the night. To simulate diurnal wind speeds, a random component (normally distributed) with a diurnally varying standard deviation was added to the point scatterer positions. This standard deviation is plotted in Fig. 11. The time series for a scene with this diurnally varying geometry, but constant backscatter, is shown in Fig. 12 (bottom left). During periods with large geometric fluctuations (high wind speeds), the variance between the 50 forest realizations is small. If the diurnal backscatter component is added, the time series take the forms shown in Fig. 12 (bottom right). The correct backscatter variations are seen during the day when the geometry fluctuates. During the night, the backscatter will recover to a value with a large amount of speckle variance.

The simulation results show that the correct temporal variations in backscatter are observed when:

- Case 1 geometric fluctuations are small for several hours (top left plot in Fig. 12);
- Case 2 geometric fluctuations are large for several hours (top right plot in Fig. 12).

When geometric fluctuations vary significantly during the day, the time series might not show the true physical variation in backscatter. The variance of unsmoothed observed time series over a 4-h period was used to determine whether the time series show the correct physical variation in backscatter. The simulated relationship between this variance and the 90% confidence interval of speckle variations is shown in Fig. 13. There is little change in the confidence interval below a backscatter variance of 0.1 dB, and thus 0.1 dB was adopted as the upper threshold for detecting Case 1 in the observed time series. During windy conditions, the 90% confidence interval of speckle variations is below 0.5 dB for a backscatter variance of 0.38 dB and higher, which is sufficient for observing backscatter fluctuations on the order of 1 dB. A variance of 0.38 dB was thus adopted as a lower

threshold for detecting Case 2. Segments of time series detected as Case 1 or Case 2 have a high likelihood of showing the true physical backscatter variation.

## IV. RESULTS

The time series results in this section are presented in the order of longest time scales and largest backscatter variations to smaller backscatter variations at shorter time scales.

### A. Long-Term Variations

The temporally smoothed backscatter time series are shown in Fig. 14 along with air temperature, precipitation, and soil moisture content. The backscatter from the canopy, ground, and full forest ROIs are plotted on the same axes for each polarization. The largest temporal variations occurred during the winters when the air temperature dropped below 0 °C. The freeze–thaw backscatter variations were largest for the canopy region, with more than 10-dB variations observed for all polarizations. The full forest freeze–thaw variations for HH and VV were similar to one another, differing mainly in amplitude. HH variations during the winter (up to 8 dB) are larger than those of VV (up to 5 dB). Winter variations in full forest VH backscatter (up to 10 dB) were larger than those of the co-pol channels because of the stronger contribution of the canopy to the full forest backscatter. The HH and VV ground-level backscatter time series were similar to those of the full-forest backscatter since the ground backscatter variations dominated the copolarized full forest backscatter during the winters.

HH and VV full forest backscatter showed similar temporal dynamics throughout the rest of the observation period as well. Smaller variations over a range 3 to 5 dB at timescales of weeks to months can be observed for HH and VV during autumn 2017 and spring/summer 2018, which show some correlation with soil moisture. VH does not show long-term variations that are correlated with soil moisture. This is due to the stronger double-bounce scattering at HH and VV, which is affected by soil moisture. The ground-level backscatter dynamics for HH and VV were similar to one another, showing some correlation with soil moisture content during nonfrozen conditions. These ground level variations were larger for HH compared to VV, likely as a result of stronger ground and stem reflections at HH due to the Brewster effect. These observations confirm that the copolarized backscatter variations are strongly influenced by double-bounce scattering, which appears at the ground level. Soil moisture changes appear to be the dominant cause of long-term variations in the ground-level and full forest HH and VV backscatter during nonfrozen conditions. The ground-level VH backscatter differs significantly from the full forest VH backscatter. This is because ground-level scattering, such as double-bounce scattering, is smaller for VH and therefore has little influence on the full forest VH backscatter. The ground-level VH backscatter showed some freeze–thaw effects, but otherwise erratic variations. These variations are amplified by the decibel scale since the ground-level backscatter is relatively low for VH due to significant attenuation by the canopy and little double-bounce scattering.



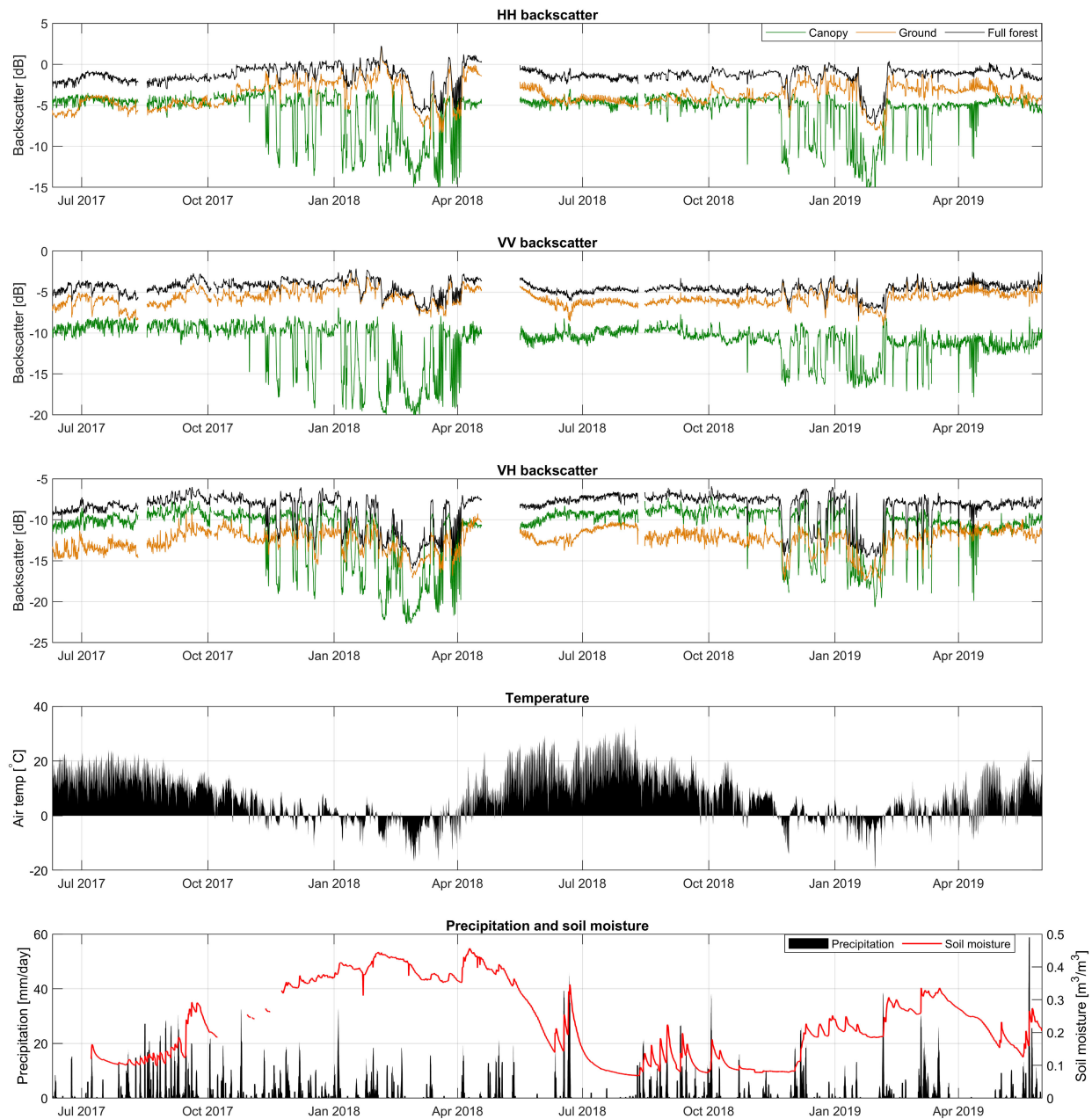


Fig. 14. Time series of the temporally smoothed forest backscatter for the three ROIs and three polarization combinations. The air temperature, precipitation, and volumetric soil moisture content are shown in the bottom two plots.

During nonfrozen conditions, the canopy backscatter was stable on the long term for all polarizations, especially for HH and VV. VH canopy backscatter does not show a significant improvement in stability compared to the full-forest backscatter since the canopy contribution dominates the full forest backscatter. The similarity in canopy-level backscatter dynamics between polarizations indicates that the underlying scattering mechanism is independent of polarization. This mechanism is volume scattering, in which the scattered electric field is the coherent sum of contributions of many, randomly orientated scattering elements within a resolution cell. This makes the canopy-level backscatter independent of soil moisture content. The only significant difference seen between polarizations is that the VH canopy backscatter exhibits a seasonal component

with a peak-to-peak amplitude of approximately 2 dB during nonfrozen conditions. This is shown in Fig. 15. The cause of this seasonal backscatter cycle, which is only visible for VH, is not clear from the available data. Possible causes could be seasonal moisture variations, tree ring formation, or reproduction cycles. The long-term periodicity makes it unlikely that these cycles are a result of speckle variance.

Satellites in a dawn/dusk polar orbit will only observe around 6:00 and 18:00. Fig. 16 shows the histograms of the full forest backscatter for all observations, dawn only and dusk only. Dawn observations included all observations between 5:30 and 6:30. Dusk observations included observations from 17:30 to 18:30. For any given polarization, there is no significant difference in the backscatter distributions when considering dawn or dusk

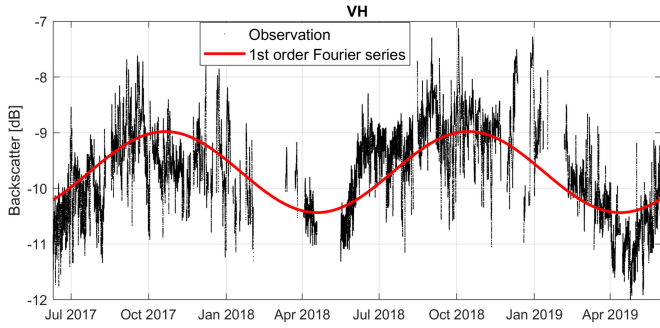


Fig. 15. VH canopy backscatter and a 1st-order Fourier series fit showing a seasonal component. Frozen conditions were manually removed from the backscatter data.

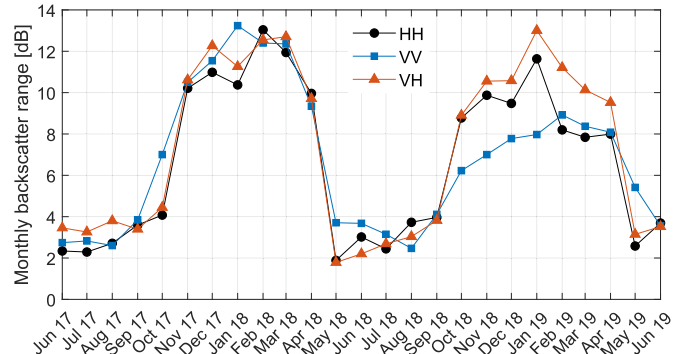


Fig. 17. Monthly range of the canopy backscatter. The winter periods show the largest range of canopy intensities due to freeze–thaw cycles and do not vary significantly between polarizations, except for VV in the winter of 2018–2019.

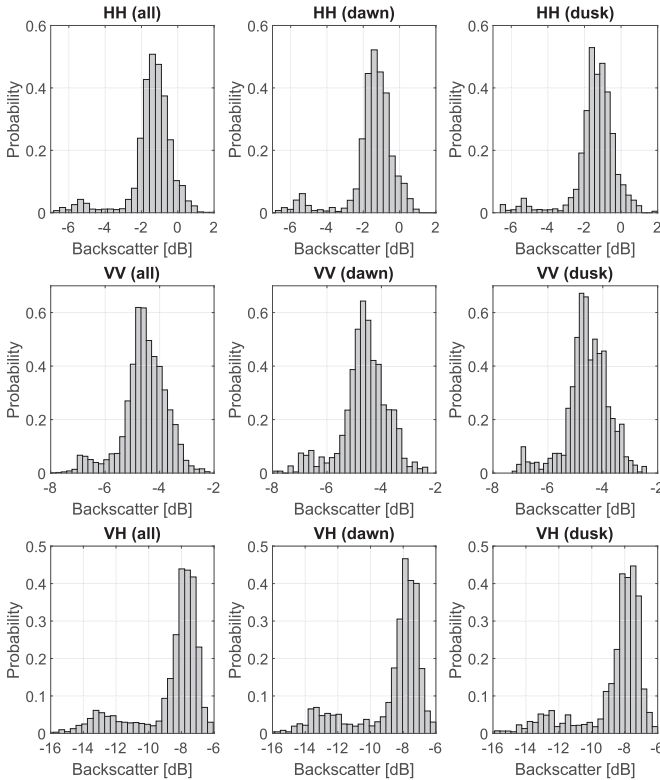


Fig. 16. Histograms showing the distributions of full forest backscatter when considering all observations (left column), dawn observations only (middle column), and dusk observations only (right column). Dawn was defined as from 5:30 to 6:30 and dusk was defined as from 17:30 to 18:30.

only. This is because backscatter variations over timescales longer than 1 d dominate the full forest backscatter time series for all polarizations. In HH and VV these variations appear to originate from changes in the ground level backscatter. For VH, the source of long-term variations is not clear and may partly be due to speckle variance.

**B. Effects of Freeze–Thaw Cycles**

Freeze–thaw cycles cause the largest variations in P-band canopy backscatter. This is most clearly seen in the monthly peak-to-peak backscatter range shown in Fig. 17. The canopy backscatter range has a seasonal cycle, reaching up to 13-dB

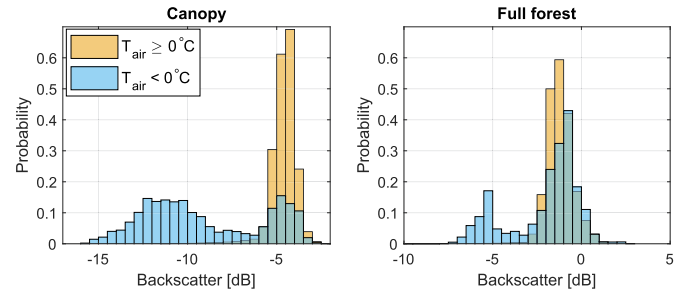


Fig. 18. Histograms showing the HH backscatter distributions for temperatures above and below 0 °C for the entire observation period. Other polarizations show similar distribution differences.

during the winter. There is no significant difference between polarizations, except that the canopy backscatter range for VV is lower than that of other polarizations during the early winter of 2018–2019. This is likely due to the warmer temperatures of the 2018–2019 winter.

The canopy backscatter is significantly lower during freezing temperatures, as is shown by the HH canopy backscatter distributions in Fig. 18. This is because part of the free water in the trees turns into ice, which has a significantly lower permittivity compared to liquid water [45], [46], resulting in weaker reflections of electromagnetic waves. The distribution of canopy backscatter during freezing temperatures is bi-modal, showing that the vegetation does not freeze at the exact onset of subzero air temperatures. This may be due to a difference in air and tree temperatures or because free water in vegetation may exist in a supercooled state before ice nucleation occurs [30], [47], [48]. Canopy and full forest backscatter were comparably stable during nonfrozen conditions, with a standard deviation of 0.7 to 1 dB.

A sample of the HH backscatter time series during the winter is shown in Fig. 19 for closer inspection. The canopy backscatter drops significantly (up to 10 dB) when the air temperature drops from positive to negative temperatures. Moisture in the canopy freezes rapidly, making the canopy more transparent to a P-band radar. This is true for all polarizations. The reduced canopy attenuation during freezing temperatures results in an increase in ground-level backscatter at the onset of negative temperatures.

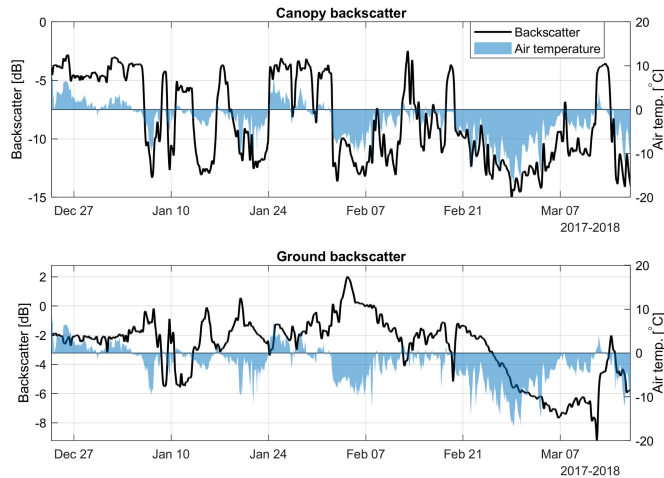


Fig. 19. Canopy and ground-level tomographic backscatter for HH-polarization during freeze–thaw cycles. Canopy backscatter drops significantly during freezing temperatures. Ground-level backscatter is stronger in freezing temperatures because the canopy attenuation is lower. For sustained freezing temperatures, the ground backscatter eventually decreases as it freezes from the top down.

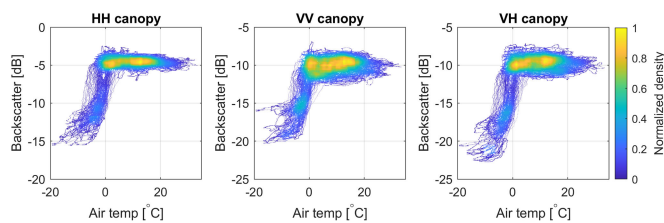


Fig. 20. Scatterplots of the canopy backscatter versus air temperature. For temperatures below 0 °C, a strong correlation between air temperature and canopy backscatter exists due to varying ice fractions in the trees.

Canopy and ground-level backscatter for HH and VV counteract one another during freeze–thaw cycles. As a result, the full forest backscatter, which is the sum of the canopy and ground-level reflections, shows little freeze–thaw variation for much of the winter (see Fig. 14). However, during sustained negative air temperatures, the ground and lower tree trunks gradually freeze, reducing the double-bounce scattering and lowering the ground-level backscatter (February–March 2018 in Fig. 19). This leads to large drops in full-forest backscatter during the winter. Freeze–thaw cycles for HH and VV have a significant impact on tomographic P-band SAR, but the full-forest backscatter is only affected during sustained negative air temperatures. For VH, canopy scattering dominates the full-forest backscatter, causing large variations in both canopy and full-forest backscatter during freeze–thaw cycles.

A strong positive correlation is observed between canopy backscatter and air temperature during freezing conditions in the scatterplots in Fig. 20. The dielectric properties of ice have a negligible temperature dependence below 0 °C [49], [50], and do not cause the observed backscatter variations. Instead, these observations are due to a varying fraction of free water in the trees which turns into ice [51]. The ice fraction of wood, and thus its permittivity, is strongly temperature dependent for subzero temperatures [52].

The freeze–thaw dynamics of the ground-level backscatter are more complicated because canopy freezing, stem freezing, and ground freezing do not necessarily occur at the same time. Spatio-temporal ice formation mechanisms in trees are not well understood and the role of ground freezing in the observed freeze–thaw dynamics is not clear from this study. Our results agree with previous studies that the canopy freezes first [30], [53], after which the lower trunk gradually freezes over the timescale of hours. Ground backscatter exhibits polarization-dependent hysteresis during freeze–thaw cycles [54]. However, the freezing dynamics in the trunks and soil cannot be separated in tomographic imaging, complicating the modeling, and interpretation of ground-level freeze–thaw dynamics.

### C. Effects of Snow Cover and Melting Snow

The upper canopy backscatter does not appear to be affected by snow. Surveillance camera footage showed that snow collecting on branches caused the branches to sag. This change in geometry had no observable effect on the upper-canopy backscatter since the branches were mostly transparent to P-band radar during subzero air temperatures. The upper canopy backscatter changes were instead more clearly correlated with temperature variations, which through the canopy attenuation affects the ground-level backscatter. Snow that collected on the ground (10 cm) also had no distinguishable effect on ground-level backscatter.

The effect of melting snow is difficult to examine since it is usually accompanied by an air temperature change from negative to positive degrees Celsius, which dominates backscatter variations. Rain is often the cause of snow melting on the ground, which causes a clear increase in ground-level backscatter in channels where the ground plays a significant role (HH and VV). HH and VV backscatter were closely correlated with soil moisture content when the snow was melting. Snow on the ground melting in the absence of rain did not show any significant change in ground-level backscatter.

These results suggest that snow has no significant effect on P-band radar observations of the studied forest site. However, this site did not experience long-term heavy snowfall during the observation period, leaving these results inconclusive.

### D. Diurnal Variations

Backscatter variations on diurnal timescales were observed during the summers. Fig. 21 shows an example of diurnal backscatter cycles for HH during the hot summer of 2018, along with the VPD. The canopy backscatter was consistently lower during the day and higher during the night. The period shown in Fig. 21 was mostly detected as Case 1, implying that the unsmoothed canopy backscatter time series had a variance that was small enough, such that speckle variations over time are negligible (see Section III-D). Therefore, there is a high likelihood that the canopy backscatter time series show true physical variations for this period. Similar diurnal backscatter variations were observed for all polarizations (see Fig. 22), during all three summers, and in a tropical forest by the TropiScat

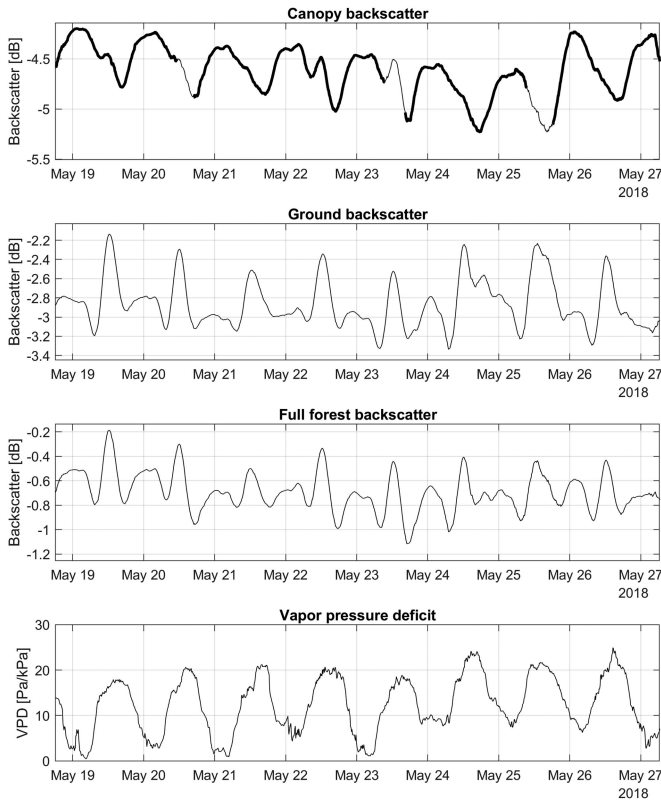


Fig. 21. Diurnal cycles in HH backscatter during the summer of 2018. A high VPD indicates high rates of transpiration, making the canopy lose moisture. This reduces the backscattered power from the canopy and reduces canopy attenuation, increasing double-bounce scattering seen at the ground level. The tick marks corresponds to midnight each day. The thick lines in the top plot mark time series segments detected as Case 1 (see Section III-D), where speckle variance is low and the observed temporal variations are likely due to a change in the scattering intensity of all scatterers in the region of interest.

experiment [2], further suggesting that the observed variations are true physical variations.

The VPD reaches high values around noon, which is an indication of a high rate of transpiration. During these high rates of transpiration, a decrease in canopy backscatter is observed, increasing again in the evening. This canopy backscatter decrease is likely due to a decrease in tree water content in the upper canopy. The diurnal patterns for HH and VV were very similar, suggesting similar diurnal scattering mechanisms. The HH and VV ground backscatter showed a sharp increase around noon, which may be connected with stomatal closure. Stomatal closure occurs when the VPD is very high and trees risk undergoing permanent damage whereby the water columns in xylem vessels break apart due to low pressures, becoming air-filled (cavitation) [55]. To regulate this pressure, trees may close their stomata in the middle of the day, limiting transpiration and halting the decrease in tree water content [56]. Midday stomatal closure may also be the cause of the bump around noon in the canopy backscatter seen in Fig. 22.

Diurnal cycles, as are shown in Figs. 21 and 22, were most clearly visible during periods with favorable atmospheric conditions for transpiration. Such conditions include warm air

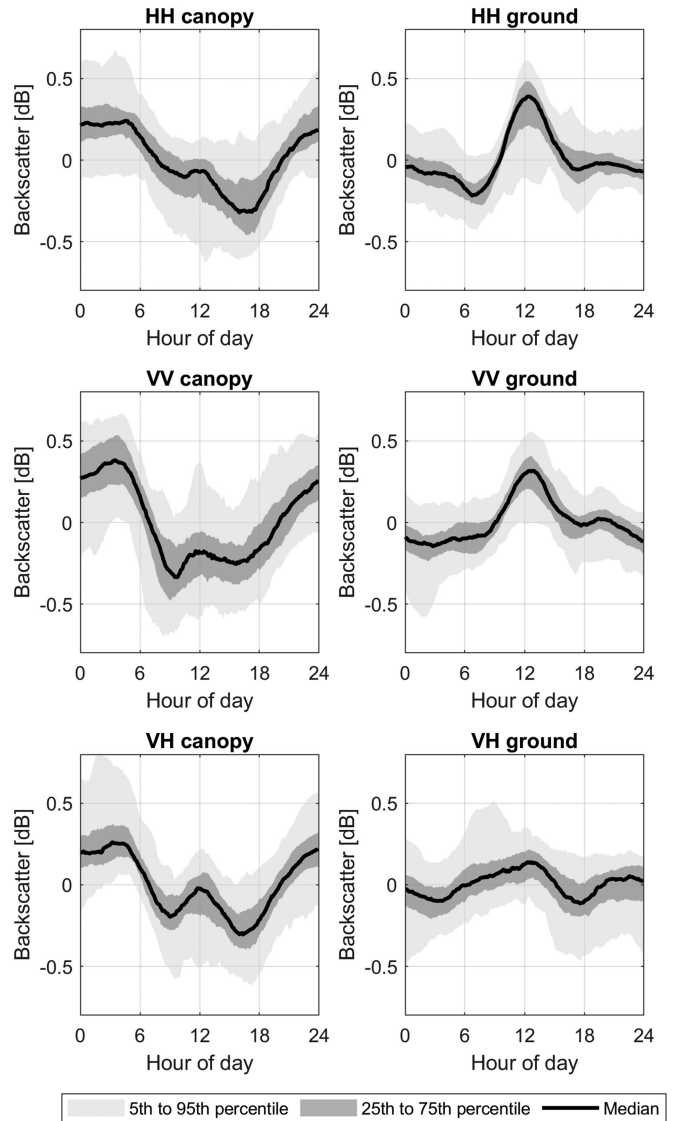


Fig. 22. Diurnal cycles for the summer period of 17 May 2018 to 9 August 2018. All polarizations show a decrease in canopy backscatter during the day when the transpiration rate is highest. Only HH and VV show a clear ground backscatter increase around noon. The daily mean was subtracted from each daily segment before producing the statistics shown.

temperatures, low relative humidity, unobstructed sunlight, and moderate-to-high wind speeds [28], [29]. Diurnal cycles were not observed during the autumns and winters. Diurnal backscatter variations with similar peak-to-peak amplitudes (1 dB) and the same diurnal phases were observed in a tropical forest for HH, VV, and HV, but only during the dry season [2]. In hot and dry conditions, the rate of transpiration exceeds the rate of water uptake by the roots in the morning, resulting in a depletion of the tree’s internal water reserves [26], [27], [57]. The water reserves are replenished again during the evening and night through water uptake by the roots when the rate of transpiration decreases, i.e., the rate of root water uptake exceeds the rate of transpiration. The tree water reserves are believed to serve as a buffer between root water uptake and water released to the atmosphere through

transpiration to avoid permanent damage by cavitation [26]. Water reserves are believed to reside in the bark and sapwood. It is the decrease of water within these tissues which may be the cause of the observed decrease in canopy backscatter during hot days. The refilling of water reserves during the evenings and nights may then be the cause of the higher backscatter during these times compared to during the day. These observations indicate that P-band radar measurements of forests are sensitive to the diurnal transpiration cycles in boreal forests and that, under certain environmental conditions, biophysiological variables such as transpiration rate and tree water content may be sensed using P-band radar.

### E. Effects of Rain

During rainfall, much of the rain is intercepted by the forest canopy in this dense forest. This increase in water on the canopy can be expected to have an effect on the observed backscatter. Studies have shown that rainfall can also lead to an increase in the permittivity of trees, while some rainfall events have no effect [58], [59]. The effect of rain during the summer of 2018 is shown in Fig. 23. During the three heavy rainfall periods (A, B, and C in Fig. 23), the canopy backscatter increased notably for HH and VV (1 to 2 dB). This suggests that the intercepted rainfall increases canopy backscatter due to an increase in water on the canopy. One can also expect an increase in canopy attenuation, leading to a decrease in ground-level backscatter during heavy rain. Such a drop in ground-level backscatter was only clearly seen for VV in Fig. 23, whereas the ground-level backscatter for HH seemed to increase by a small amount during rain. The rainfall events were accompanied by large increases in soil moisture at the ground surface. Such an increase in soil moisture should affect both HH and VV ground-level backscatter with approximately the same magnitudes since the soil Fresnel reflection coefficients for both horizontally and vertically polarized waves at oblique incidence increase by approximately the same magnitudes with an increase in soil moisture [41]. The difference between the behavior of HH and VV ground-level backscatter during heavy rainfall may be due to different canopy attenuation mechanisms, whereby heavy rainfall increases the canopy attenuation for VV more than for HH, but speckle may also have a dominant effect during rainfall.

The light rainfall events (D and E in Fig. 23) did not have any significant effect on the observed backscatter. Since heavy rainfall such as events A, B, and C in Fig. 23 were rare in this region, rain rarely had any noticeable effect on tomographic image backscatter at P-band. Events A, B, and C in Fig. 23 should therefore be considered as extreme cases.

### F. Effects of Wind

Wind causes geometric changes in the observed scene as trees sway in the wind. These geometric changes cause fluctuations in the observed backscatter. Fig. 24 shows the observed canopy backscatter with and without temporal averaging (smoothing) as well as the average wind speed for a period during the 2017 summer. During periods with strong winds ( $>5$  m/s), large

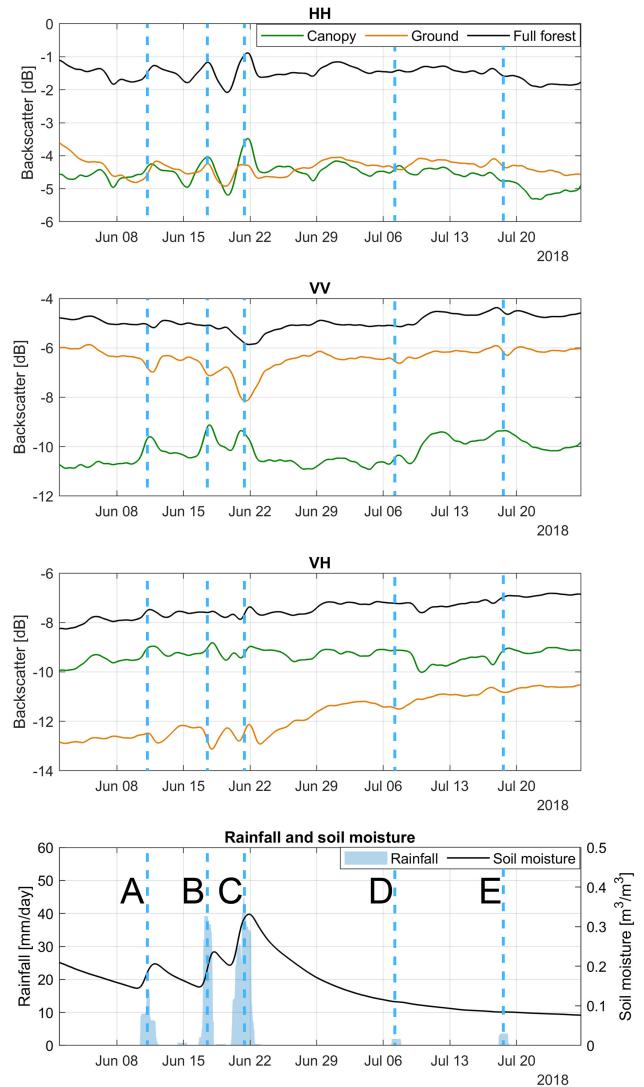


Fig. 23. Canopy, ground-level, and full forest backscatter time series along with the rainfall. The dashed blue lines and labels A to E mark the times at which rainfall occurs. The time series were smoothed to remove diurnal variations. Heavy rain has a clear effect on canopy and ground-level backscatter whereas light rain does not have any significant effect.

backscatter fluctuations over timescales of hours can be seen. This is temporal speckle, or Rayleigh fading, which occurs when the scattered fields from scattering elements in the forest interfere constructively and destructively over time. This is true for all polarizations. During summer nights and mornings, there was little wind, making the backscatter very stable over timescales of hours.

The temporally averaged backscatter time series in Fig. 24 also show that strong winds coincide with a 1 to 2-dB drop in average canopy backscatter. This is most common in segments detected as Case 2, meaning that the wind causes a large amount of temporal speckle and that the smoothed time series show the true physical backscatter variations larger 0.5 dB (see Section III-D). Similar to diurnal cycles observed during windless conditions, these drops in backscatter usually occur during

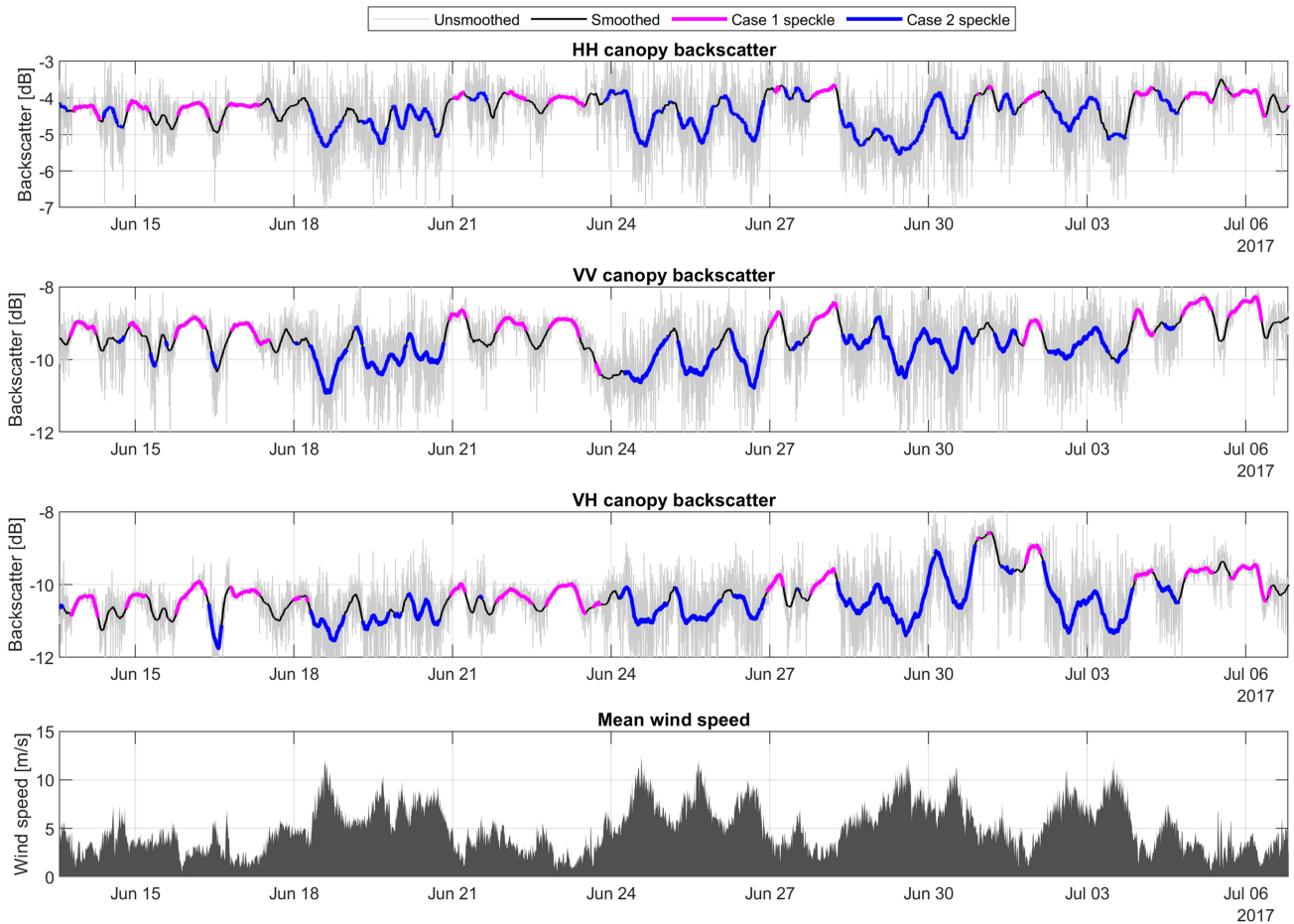


Fig. 24. Time series of the canopy backscatter and wind speed during the 2017 summer. Strong winds cause both short-term fluctuations in backscatter and a drop in mean backscatter. Regions detected as Case 1 and Case 2 (see Section III-D) are shown by magenta and blue curves, respectively.

the day, with the backscatter increasing again during the night, even during Case 2 conditions (e.g., 30 June 2017). The observed drops in the smoothed canopy backscatter time series are, therefore, not due to speckle. A similar drop in full forest backscatter was previously observed in nontomographic measurements [4], which was attributed to decreased double-bounce scattering as the trees bend in the wind. The motivation for this interpretation was that the drop in backscatter was not seen for VH polarization, which is less sensitive to double-bounce scattering. However, the tomographic data shows that a drop in the canopy backscatter during high wind speeds, as in Fig. 24, occurs for all polarizations. Since the relationship between canopy backscatter and wind speed is not one-to-one, they are best compared with their rates of change with time, as is shown in Fig. 25. An increase in wind speed appears to cause a decrease in the canopy backscatter of HH, VV, and VH, and an increase in the ground backscatter of VH. The ground backscatter of HH and VV was insensitive to wind speed. This increase in VH ground backscatter is likely due to increased double-bounce scattering between the bending stems and the ground [60], counteracting the decrease canopy backscatter during windy conditions. This explains why the effect was not seen in [4] for cross-polarized full forest backscatter. These results show that a change in double-bounce scattering

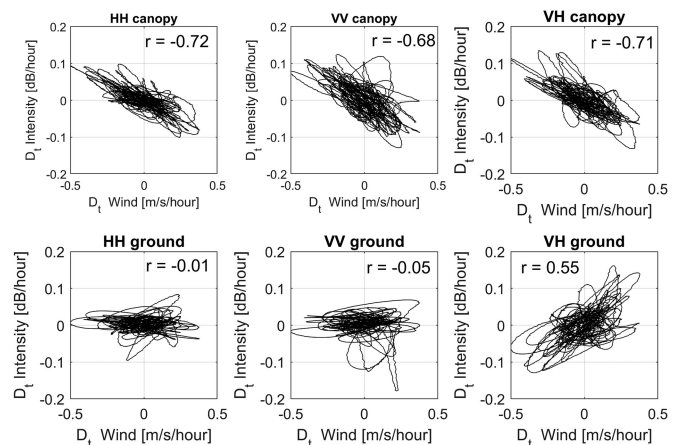


Fig. 25. Time derivative of the mean backscatter versus the derivative of wind speed. The correlation coefficient  $r$  is given in each plot. The canopy backscatter decreases when wind speed increases. The opposite behavior is seen for VH ground-level backscatter.

is not the sole underlying mechanism behind the decrease in backscatter during strong winds. A more likely cause of the observed drop in canopy backscatter is a decrease in water

content in the canopy during windy summer days. When trees transpire, the air at the leaf/needle surface becomes saturated with water vapor from the stomata, decreasing the VPD at the leaf surface and reducing the rate of transpiration [56], [61]. Wind replaces this saturated air with dry air, increasing the VPD at the stomata and increasing the rate of transpiration [62], [63]. The high rate of transpiration during strong winds decreases the tree water content, causing a decrease in canopy backscatter during the day.

These results suggest that wind causes a decrease in the mean canopy backscatter with the same mechanism causing diurnal cycles during hot periods: High rates of transpiration causes a depletion of the tree's water reserves during the day, decreasing the backscatter. This theory is supported by the observation that strong winds during cold conditions did not cause a decrease in mean canopy backscatter. Strong winds during periods with little solar radiation will cool the stomata, decreasing the rate of transpiration [62]. The rate of transpiration will also be low if the relative humidity is high, such as during rainy periods. During cold or humid conditions, depletion of the tree's internal water reserves is not necessary to sustain the low rate of transpiration driven by the atmospheric conditions.

## V. DISCUSSION

The largest backscatter variations observed were caused by freezing temperatures. The large drops in canopy (as well as full forest) backscatter during frozen conditions may result in large errors in forest parameter estimates and forest disturbance detections using P-band SAR data. The multidecibel backscatter variations observed during the winter will result in boreal forest biomass estimation errors well above the specified 20% for BIOMASS [64]. Correcting for this drop is not simple since the permittivity of wood is strongly dependent on temperature during frozen conditions. The best approach would be to discard SAR observations acquired during frozen conditions, but this requires frozen conditions to be detected. Such a detection is complicated by the observation that the drop in backscatter does not occur until a few degrees below 0 °C, and thawing may not occur until several degrees above 0 °C. Therefore, air temperature cannot be used as a reliable proxy. Another complication is that while the canopy may be frozen, the effect might not be seen in the full forest HH and VV backscatter as observed by a single SAR overpass. However, this was not the case for cross-polarized observations. Therefore, the best possibility for detecting frozen conditions from backscatter data would be to detect changes (>2 dB) in cross-polarized backscatter between SAR overpasses. Large drops in cross-polarized backscatter, which do not appear in copolarized backscatter, are likely due to frozen trees during the time of overpass and not deforestation. However, during sustained frozen conditions, the copolarized channels will also show a drop in backscatter (see Fig. 14). Therefore, this approach is questionable for other forest densities and climates. The possibility of using phase shifts for detecting freezing conditions should be investigated in the future.

HH and VV full forest backscatter were influenced by large variations in ground-level backscatter (3 to 5 dB) due to soil moisture changes. HH appeared most sensitive to soil moisture variations. The corresponding variations in the full forest backscatter were smaller since the canopy contributed significantly to the full forest backscatter in this dense forest. In forests of lower density, with less canopy backscatter and attenuation, soil moisture variations can be expected to play a larger role in full forest HH and VV backscatter. Canopy backscatter was very stable over long timescales if frozen periods are excluded (see Fig. 14). Therefore, canopy backscatter will be accurately rendered by repeat-pass SAR tomography and ground-notching interferometry, assuming high temporal coherence. These results support the current approaches for biomass estimation using P-band SAR.

A 0.5-dB difference in canopy backscatter can be expected between 6 A.M. and 6 P.M. overpasses (see Fig. 22). The long revisit times of polar-orbiting, sun-synchronous SARs makes them unable to capture the full diurnal dynamics of forest backscatter. Diurnal variations in canopy backscatter were connected to the current understanding of tree water relations. The canopy backscatter diurnal cycles resemble the temporal signatures of stem radii as measured by dendrometers. These cycles can be described as a constant value that dips during the day. However, radar backscatter is more closely related to permittivity than stem radius. Diurnal variations in stem permittivity are more sinusoidal than those measured by dendrometers [46], [58]. This discrepancy may partially be explained by the nonlinear relationship between permittivity and backscatter [20]. The relationship between canopy backscatter and the permittivity measured at a single point in a stem may also be more complicated than what is currently accepted. To the authors' knowledge, no experimental work has been carried out in which both backscatter and permittivity were measured over diurnal timescales. Time series of the *in situ* permittivity of upper canopy structures have also not been acquired yet.

Short-term fluctuations in backscatter due to wind are not expected to significantly affect P-band SAR observations. Spatial multilooking in SAR images can be used to average and reduce these fluctuations. However, repeat-pass techniques such as interferometry and tomography will be affected by these fluctuations in the form of temporal decorrelation. It was also observed that strong winds may cause a canopy backscatter drop of up to 2 dB during warm periods. These drops in mean backscatter coincided with a large amount of speckle variation. A multichannel speckle filter based on samples from multiple times and polarizations was also tested [65]. The smoothed time series were not significantly affected by this filter due to the dense multitemporal averaging capacity of the data. Therefore, the filter was not included in the results presented in this article. The observed drops in backscatter may cause a difference in the backscatter observed during 6 A.M. overpasses compared to 6 P.M. overpasses and may result in minor errors in forest parameter estimates. However, strong winds during hot conditions are rare in boreal forests.

## VI. CONCLUSION

In this study, a mature stand of Norway spruce was monitored by a multipolarimetric, tomographic tower-based radar over a two-year period. Time series of the forest backscatter, ground-level backscatter, and upper-canopy backscatter were extracted from tomographic images and analyzed in relation to meteorological variables. The largest temporal variations in backscatter were due to freezing temperatures in the winter. Such variations will lead to large forest parameter estimates if not compensated for or excluded. The canopy backscatter, which is the most sensitive to forest biomass, showed the largest changes in backscatter (10-dB drops) during freezing temperatures. Ground backscatter only dropped during sustained freezing conditions. During nonfrozen conditions, the canopy backscatter was observed to be more stable than the ground and backscatter for all polarizations due to decreased sensitivity to soil moisture changes. Cross-polarized full forest backscatter was dominated by the canopy contribution, showing similar temporal variations during nonfrozen conditions. Observations during dawn or dusk times did not show a decrease in temporal backscatter variations. Diurnal variations (1 dB) were observed during hot periods and even larger variations (up to 2 dB) were observed during strong winds in the summer. These phenomena appeared to be connected to high transpiration rates that result in a decrease in tree water content during the day.

Regarding the diurnal backscatter variations observed, information about the water transport in forests is important for ecophysiology, soil water dynamics, and the management of watersheds. Tower-based radars could be used as a new research tool for characterizing tree water content signatures over spatial scales of forest stands to ecosystems. Changes in tree water content can be used to constrain canopy conductance, which is a key variable in soil-vegetation-atmosphere transport models, ecosystem productivity models, and global climate models [66]. Although only a single tree species was observed in this study, trees of different species have very similar diurnal characteristics of water transport [67], and can be expected to show similar backscatter signatures. The magnitude of backscatter variations due to tree water content variations is still uncertain and thus, our interpretation of the observed diurnal cycles is speculative.

It is concluded that several questions remain to be addressed. The origin of canopy-level backscatter is not clear for the different polarizations. A decrease in canopy backscatter did not always appear to coincide with an increase in ground backscatter (e.g., through a reduction of canopy attenuation). Separation of backscatter contributions from different regions in the forest is difficult even with tomographic radar. Changes in ground-level backscatter, which has a significant influence on HH and VV full forest backscatter, can be caused by canopy attenuation, stem water content, or soil moisture content variations. These effects could not be separated in this study, complicating the interpretation of the effects of freeze–thaw cycles, strong winds, and rain. It is also concluded that future work should include the analysis of backscatter data along with dendrometer, sap flow, and soil moisture profile data. Measurements of the *in situ* permittivity will also be made since there is a possibility that the

stem water content and permittivity can be affected by chemical changes [58], [68]. Measurements of the complex permittivity will also clarify the relationship between backscatter and attenuation in forest canopies. Finally, a similar analysis for the phase evolution over time and for observations at other frequency bands (e.g., L-band and C-band) will be done, providing deeper insight into the electromagnetic scattering mechanisms and temporal backscatter variations throughout the forest canopy.

## ACKNOWLEDGMENT

The authors would like to thank the Swedish Defence Research Agency (FOI) for providing and installing the trihedral corner reflectors at the experimental site, the Swedish University of Agricultural Sciences (SLU) for providing the terrestrial lidar point cloud of the forest site, the European Space Agency (ESA) for funding the BorealScat experiment, and also the two anonymous reviewers for their constructive input.

## REFERENCES

- [1] C. Albinet, P. Borderies, N. Floury, and E. Pottier, "Measure of temporal variation of P-band radar cross section and temporal coherence of a temperate tree," *IEEE Trans. Geosci. Remote Sens.*, vol. 54, no. 11, pp. 6255–6264, Nov. 2016.
- [2] A. Hamadi *et al.*, "Temporal survey of polarimetric P-band scattering of tropical forests," *IEEE Trans. Geosci. Remote Sens.*, vol. 52, no. 8, pp. 4539–4547, Aug. 2014.
- [3] J. T. Pulliainen, L. Kurvonen, and M. T. Hallikainen, "Multitemporal behavior of L- and C-band SAR observations of boreal forests," *IEEE Trans. Geosci. Remote Sens.*, vol. 37, no. 2, pp. 927–937, Mar. 1999.
- [4] A. R. Monteith and L. M. H. Ulander, "Temporal survey of P- and L-band polarimetric backscatter in boreal forest," *IEEE J. Sel. Topics Appl. Earth Observ. Remote Sens.*, vol. 11, no. 10, pp. 3564–3577, Oct. 2018.
- [5] "Report for mission selection: BIOMASS," Eur. Space Agency, Noordwijk, The Netherlands, ESA SP-1324/1, 2012.
- [6] S. Quegan *et al.*, "The European space agency BIOMASS mission: Measuring forest above-ground biomass from space," *Remote Sens. Environ.*, vol. 227, pp. 44–60, 2019.
- [7] T. Le Toan, A. Beaudoin, J. Riou, and D. Guyon, "Relating forest biomass to SAR data," *IEEE Trans. Geosci. Remote Sens.*, vol. 30, no. 2, pp. 403–411, Mar. 1992.
- [8] M. C. Dobson, F. T. Ulaby, T. Le Toan, A. Beaudoin, E. S. Kasischke, and N. Christensen, "Dependence of radar backscatter on coniferous forest biomass," *IEEE Trans. Geosci. Remote Sens.*, vol. 30, no. 2, pp. 412–415, Mar. 1992.
- [9] H. Israelsson, J. Askne, and R. Sylvander, "Potential of SAR for forest bole volume estimation," *Int. J. Remote Sens.*, vol. 15, no. 14, pp. 2809–2826, 1994.
- [10] S. H. Alemohammad, T. Jagdhuber, M. Moghaddam, and D. Entekhabi, "Soil and vegetation scattering contributions in L-band and P-band polarimetric SAR observations," *IEEE Trans. Geosci. Remote Sens.*, vol. 57, no. 11, pp. 8417–8429, Nov. 2019.
- [11] F. Banda *et al.*, "The BIOMASS level 2 prototype processor: Design and experimental results of above-ground biomass estimation," *Remote Sens.*, vol. 12, no. 6, 2020, Art. no. 985.
- [12] J. M. B. Carreiras *et al.*, "Coverage of high biomass forests by the ESA BIOMASS mission under defense restrictions," *Remote Sens. Environ.*, vol. 196, pp. 154–162, 2017.
- [13] M. J. Soja, G. Sandberg, and L. M. H. Ulander, "Regression-based retrieval of boreal forest biomass in sloping terrain using P-band SAR backscatter intensity data," *IEEE Trans. Geosci. Remote Sens.*, vol. 51, no. 5, pp. 2646–2665, May 2013.
- [14] D. H. T. Minh *et al.*, "SAR tomography for the retrieval of forest biomass and height: Cross-validation at two tropical forest sites in French Guiana," *Remote Sens. Environ.*, vol. 175, pp. 138–147, 2016.
- [15] S. Tebaldini and F. Rocca, "Multibaseline polarimetric SAR tomography of a boreal forest at P- and L-bands," *IEEE Trans. Geosci. Remote Sens.*, vol. 50, no. 1, pp. 232–246, Jan. 2012.



- [16] M. J. Soja, M. M. d'Alessandro, S. Quegan, S. Tebaldini, and L. M. H. Ulander, "Model-based estimation of tropical forest biomass from notch-filtered P-band SAR backscatter," in *Proc. IEEE Int. Geosci. Remote Sens. Symp.*, Jul. 2018, pp. 8617–8620.
- [17] M. J. Soja *et al.*, "Mapping above-ground biomass in tropical forests with ground-cancelled P-band SAR and limited reference data," *Remote Sens. Environ.*, to be published.
- [18] F. T. Ulaby, "Radar response to vegetation," *IEEE Trans. Antennas Propag.*, vol. 23, no. 1, pp. 36–45, Jan. 1975.
- [19] E. Puttonen *et al.*, "Quantification of overnight movement of birch (*Betula pendula*) branches and foliage with short interval terrestrial laser scanning," *Front. Plant Sci.*, vol. 7, 2016, Art. no. 00222.
- [20] M. Moghaddam, S. Durden, and H. Zebker, "Radar measurement of forested areas during OTTER," *Remote Sens. Environ.*, vol. 47, no. 2, pp. 154–166, 1994.
- [21] D. Solimini, *Understanding Earth Observation: The Electromagnetic Foundation of Remote Sensing*. Cham, Switzerland: Springer, 2016.
- [22] M. T. Hallikainen, F. T. Ulaby, M. C. Dobson, M. A. El-Rayes, and L.-K. Wu, "Microwave dielectric behavior of wet soil-Part I: Empirical models and experimental observations," *IEEE Trans. Geosci. Remote Sens.*, vol. GE-23, no. 1, pp. 25–34, Jan. 1985.
- [23] N. R. Peplinski, F. T. Ulaby, and M. C. Dobson, "Dielectric properties of soils in the 0.3–1.3-GHz range," *IEEE Trans. Geosci. Remote Sens.*, vol. 33, no. 3, pp. 803–807, May 1995.
- [24] M. Moghaddam, S. Saatchi, and R. H. Cuenca, "Estimating subcanopy soil moisture with radar," *J. Geophysical Res. Atmospheres*, vol. 105, no. D11, pp. 14 899–14 911, 2000.
- [25] H. H. Dixon and J. Joly, "On the ascent of sap," *Philosophical Trans. Roy. Soc. B*, vol. 186, pp. 563–576, 1895.
- [26] R. Zweifel, H. Item, and R. Häsler, "Link between diurnal stem radius changes and tree water relations," *Tree Physiol.*, vol. 21, no. 12/13, pp. 869–877, 2001.
- [27] S. Pfautsch, T. Hölttä, and M. Mencuccini, "Hydraulic functioning of tree stems—Fusing ray anatomy, radial transfer and capacitance," *Tree Physiol.*, vol. 35, no. 7, pp. 706–722, 2015.
- [28] P. G. Jarvis, "The interpretation of the variations in leaf water potential and stomatal conductance found in canopies in the field," *Philos. Trans. Royal Soc. London. B., Biological Sciences*, vol. 273, no. 927, pp. 593–610, 1976.
- [29] T. Kumagai, "Transpiration in forest ecosystems," in *Forest Hydrology and Biogeochemistry: Synthesis of Past Research and Future Directions*. Dordrecht, the Netherlands: Springer, 2011.
- [30] G. Charrier *et al.*, "Monitoring of freezing dynamics in trees: A simple phase shift causes complexity," *Plant Physiol.*, vol. 173, no. 4, pp. 2196–2207, 2017.
- [31] I. Hajnsek *et al.*, "BioSAR 2007: Technical assistance for the development of airborne SAR and geophysical measurements during the BioSAR 2007 experiment: Final report," Eur. Space Agency, Paris, France, Project Rep. 20755/07/NL/CB, 2008.
- [32] I. Hajnsek *et al.*, "BioSAR 2008: Technical assistance for the development of airborne SAR and geophysical measurements during the BioSAR 2008 experiment: Final report," Eur. Space Agency, Paris, France, Rep. 22052/08/NL/CT, 2010.
- [33] L. M. H. Ulander *et al.*, "BioSAR 2010: Technical assistance for the development of airborne SAR and geophysical measurements during the BioSAR 2010 experiment: Final report," Eur. Space Agency, Paris, France, Rep. 4000102285/10/NL/JA/ef, 2011.
- [34] M. Moghaddam and S. Saatchi, "Analysis of scattering mechanisms in SAR imagery over boreal forest: Results from BOREAS 93," *IEEE Trans. Geosci. Remote Sens.*, vol. 33, no. 5, pp. 1290–1296, Sep. 1995.
- [35] S. Hensley *et al.*, "UAVSAR L-band and P-band tomographic experiments in boreal forests," in *Proc. Int. Geosci. Remote Sens. Symp.*, 2018, pp. 8679–8682.
- [36] L. M. H. Ulander, A. R. Monteith, M. J. Soja, and L. E. B. Eriksson, "Multiport vector network analyzer radar for tomographic forest scattering measurements," *IEEE Geosci. Remote Sens. Lett.*, vol. 15, no. 12, pp. 1897–1901, Dec. 2018.
- [37] H. T. M. Dinh *et al.*, "Ground-based array for tomographic imaging of the tropical forest in P-band," *IEEE Trans. Geosci. Remote Sens.*, vol. 51, no. 8, pp. 4460–4472, Aug. 2013.
- [38] A. R. Monteith, L. M. H. Ulander, and S. Tebaldini, "Calibration of a ground-based array radar for tomographic imaging of natural media," *Remote Sens.*, vol. 11, no. 24, 2019, Art. no. 2924.
- [39] J. A. Goff and S. Gratch, "Low-pressure properties of water—from 160 to 212°F," *Trans. Am. Soc. Heat. Ventil. Eng.*, vol. 52, pp. 95–121, 1946.
- [40] V. Cazcarra-Bes, M. Pardini, M. Tello, and K. P. Papanthassiou, "Comparison of tomographic SAR reflectivity reconstruction algorithms for forest applications at L-band," *IEEE Trans. Geosci. Remote Sens.*, vol. 58, no. 1, pp. 147–164, Jan. 2020.
- [41] F. T. Ulaby *et al.*, *Microwave Radar and Radiometric Remote Sensing*. Ann Arbor, MI, USA: Univ. Michigan Press, 2014.
- [42] R. W. Schafer, "What is a Savitzky–Golay filter? [lecture notes]," *IEEE Signal Process. Mag.*, vol. 28, no. 4, pp. 111–117, Jul. 2011.
- [43] L. M. H. Ulander *et al.*, "Airborne SAR for calibration of P-band tower radar," in *Proc. IEEE Int. Geosci. Remote Sens. Symp.*, 2019, pp. 541–544.
- [44] J. Lee and E. Pottier, *Polarimetric Radar Imaging*. Boca Raton, FL, USA: Taylor & Francis Group, 2009.
- [45] J. Way *et al.*, "The effect of changing environmental conditions on microwave signatures of forest ecosystems: Preliminary results of the march 1988 Alaskan aircraft SAR experiment," *Int. J. Remote Sens.*, vol. 11, no. 7, pp. 1119–1144, 1990.
- [46] A. Mavrović *et al.*, "Dielectric characterization of vegetation at L band using an open-ended coaxial probe," *Geoscientific Instrum., Methods Data Syst.*, vol. 7, no. 3, pp. 195–208, 2018.
- [47] M. A. El-Rayes and F. T. Ulaby, "Microwave dielectric spectrum of vegetation-part I: Experimental observations," *IEEE Trans. Geosci. Remote Sens.*, vol. GE-25, no. 5, pp. 541–549, Sep. 1987.
- [48] H. Hänninen, *Boreal and Temperate Trees in a Changing Climate: Modelling the Ecophysiology of Seasonality*. Dordrecht, the Netherlands: Springer, 2016, vol. 3.
- [49] C. Mätzler and U. Wegmüller, "Dielectric properties of freshwater ice at microwave frequencies," *J. Phys. D: Appl. Phys.*, vol. 20, no. 12, pp. 1623–1630, 1987.
- [50] G. Hufford, "A model for the complex permittivity of ice at frequencies below 1 THz," *Int. J. Infrared Millimeter Waves*, vol. 12, no. 7, pp. 677–682, 1991.
- [51] J. P. Sparks, G. S. Campbell, and A. R. Black, "Water content, hydraulic conductivity, and ice formation in winter stems of *Pinus contorta*: A TDR case study," *Oecologia*, vol. 127, no. 4, pp. 468–475, 2001.
- [52] G. I. Torgovnikov, *Dielectric Properties of Wood and Wood-Based Materials*. Berlin, Germany: Springer-Verlag, 1993.
- [53] R. Zweifel and R. Häsler, "Frost-induced reversible shrinkage of bark of mature subalpine conifers," *Agricultural Forest Meteorol.*, vol. 102, no. 4, pp. 213–222, 2000.
- [54] U. Wegmüller, "The effect of freezing and thawing on the microwave signatures of bare soil," *Remote Sens. Environ.*, vol. 33, no. 2, pp. 123–135, 1990.
- [55] G. Bonan, *Climate Change and Terrestrial Ecosystem Modeling*. Cambridge, U.K.: Cambridge Univ. Press, 2019.
- [56] J. C. Forbes and R. D. Watson, *Plants in Agriculture*. Cambridge, U.K.: Cambridge Univ. Press, 1996.
- [57] J. Čermák, J. Kučera, W. L. Bauerle, N. Phillips, and T. M. Hinckley, "Tree water storage and its diurnal dynamics related to sap flow and changes in stem volume in old-growth Douglas-fir trees," *Tree Physiol.*, vol. 27, no. 2, pp. 181–198, 2007.
- [58] K. C. McDonald, R. Zimmermann, and J. S. Kimball, "Diurnal and spatial variation of xylem dielectric constant in Norway spruce (*Picea abies* [L.] Karst.) as related to microclimate, xylem sap flow, and xylem chemistry," *IEEE Trans. Geosci. Remote Sens.*, vol. 40, no. 9, pp. 2063–2082, Sep. 2002.
- [59] M. Watanabe *et al.*, "Multitemporal fluctuations in L-band backscatter from a Japanese forest," *IEEE Trans. Geosci. Remote Sens.*, vol. 53, no. 11, pp. 5799–5813, Nov. 2015.
- [60] T. Chiu and K. Sarabandi, "Electromagnetic scattering interaction between a dielectric cylinder and a slightly rough surface," *IEEE Trans. Antennas Propag.*, vol. 47, no. 5, pp. 902–913, May 1999.
- [61] G. Toole and S. Tool, *New Understanding Biology for Advanced Level*, 4th ed. Cheltenham, U.K.: Nelson Thornes, 1999.
- [62] F. A. Daudet, X. Le Roux, H. Sinoquet, and B. Adam, "Wind speed and leaf boundary layer conductance variation within tree crown consequences on leaf-to-atmosphere coupling and tree functions," *Agricultural Forest Meteorol.*, vol. 97, no. 3, pp. 171–185, 1999.
- [63] C. R. Chu, C.-I. Hsieh, S.-Y. Wu, and N. G. Phillips, "Transient response of sap flow to wind speed," *J. Exp. Botany*, vol. 60, no. 1, pp. 249–255, 2009.
- [64] M. Schlund, K. Scipal, and S. Quegan, "Assessment of a power law relationship between P-band SAR backscatter and aboveground biomass and its implications for BIOMASS mission performance," *IEEE J. Sel. Topics Appl. Earth Observ. Remote Sens.*, vol. 11, no. 10, pp. 3538–3547, Oct. 2018.

- [65] S. Quegan and J. J. Yu, "Filtering of multichannel SAR images," *IEEE Trans. Geosci. Remote Sens.*, vol. 39, no. 11, pp. 2373–2379, Nov. 2001.
- [66] N. G. Phillips, R. Oren, J. Licata, and S. Linder, "Time series diagnosis of tree hydraulic characteristics," *Tree Physiol.*, vol. 24, no. 8, pp. 879–890, 2004.
- [67] F. C. Meinzer, S. A. James, G. Goldstein, and D. Woodruff, "Whole-tree water transport scales with sapwood capacitance in tropical forest canopy trees," *Plant, Cell Environ.*, vol. 26, no. 7, pp. 1147–1155, 2003.
- [68] R. Gall, W. Landolt, P. Schleppi, V. Michellod, and J. Bucher, "Water content and bark thickness of Norway spruce (*Picea abies*) stems: Phloem water capacitance and xylem sap flow," *Tree Physiol.*, vol. 22, no. 9, pp. 613–623, 2002.



**Lars M. H. Ulander** (Fellow, IEEE) received the M.Sc. degree in engineering physics and the Ph.D. degree in electrical and computer engineering from Chalmers University of Technology, Gothenburg, Sweden, in 1985 and 1991, respectively.

Since 1995, he has been with the Swedish Defence Research Agency (FOI), where he is the Director of Research in Radar Signal Processing and leads the research on very high frequency/ultrahigh frequency band radar. Since 2014, he has been a Professor of radar remote sensing with Chalmers University of Technology. He has authored or coauthored over 300 professional publications, of which more than 60 are in peer-reviewed scientific journals. He is the holder of five patents. His research interests include synthetic aperture radar, electromagnetic scattering models, and remote sensing applications.



**Albert R. Monteith** (Member, IEEE) received the M.Sc. degree in electrical engineering and the Ph.D. degree in radio and space science from Chalmers University of Technology, Gothenburg, Sweden in 2015 and 2020, respectively.

He is currently a Postdoctoral Researcher with the Department of Space, Earth, and Environment. His research interest includes the temporal aspects of radar remote sensing of forests.